

# Microbiota-derived IPA protects against colitis by regulating intestinal HMGCS2-mediated ketogenesis to facilitate mucosal healing

Received: 14 May 2025

Accepted: 27 January 2026

Published online: 06 February 2026

 Check for updates

Yanan Zhang<sup>1,10</sup>, Shuyu Tu<sup>1,2,10</sup>, Xian Shao<sup>3,10</sup>, Jinxin Meng<sup>1,10</sup>, Zhuobiao Zhang<sup>1</sup>, Wei Wei<sup>4</sup>, Xuping Jing<sup>5</sup>, Zhewen Qin<sup>6,7</sup>, Jianan Wu<sup>1</sup>, Weilv Xu<sup>1</sup>, Bofei Dong<sup>7</sup>, Jinsong Gao<sup>8</sup>, Aijuan Qu<sup>9</sup>, Shuxian Chen<sup>1</sup>, Li Zhang<sup>2</sup>, Peng Gong<sup>5</sup>, Bo Shan<sup>6,7</sup>, Hui Shi<sup>1</sup> & Shu Jeffrey Zhu<sup>1,8</sup> ✉

The gut microbiota sustains intestinal homeostasis, yet how microbial metabolites direct epithelial repair remains unclear. Here we identify indole-3-propionic acid (IPA), a tryptophan-derived bacterial metabolite, as a key regulator of mucosal healing. IPA activates PPAR $\alpha$  in intestinal epithelial cells, enhancing transcription of the ketogenic enzyme HMGCS2 and boosting  $\beta$ -hydroxybutyrate (BHB) production. BHB in turn stimulates LGR5<sup>+</sup> intestinal stem cells, accelerating epithelial regeneration. Using germ-free models and the IPA-producer *Peptostreptococcus russellii*, we show that dietary tryptophan and specific commensals sustain luminal IPA levels, which are critical for recovery in colitis. Restoration of IPA or BHB attenuates inflammation and barrier defects, outlining a microbiota-metabolite-stem cell axis that could be therapeutically targeted in inflammatory bowel disease and other barrier disorders.

The intestinal epithelium serves as a critical physical barrier that separates the luminal contents from the underlying stroma. Any disruption to this barrier, whether due to infection, uncontrolled inflammation or medical interventions, must be rapidly addressed to mitigate the host's exposure to harmful luminal contents that would otherwise remain contained. In the context of severe intestinal lesions such as the crypt loss observed in inflammatory bowel disease (IBD), LGR5<sup>+</sup> intestinal stem cells (ISCs) vigorously proliferate and

differentiate to replenish the cellular pool essential for restoring the epithelial barrier, thus promoting epithelial regeneration post-injury<sup>1,2</sup>. Impaired functionality of ISCs in reestablishing the epithelial barrier is a central element in the etiology of IBD, a fact that has been well recognized and extensively studied lately<sup>3-5</sup>.

Germ-free (GF) mouse models demonstrate impaired intestinal epithelial turnover and diminished regenerative capacity upon injury<sup>6</sup>, underscoring the essential role of gut microbiota and their metabolic

<sup>1</sup>Department of Veterinary Medicine, College of Animal Sciences, Zhejiang University, Hangzhou, Zhejiang, China. <sup>2</sup>Department of Cardiology, The First Affiliated Hospital of Guangdong Pharmaceutical University, Guangzhou, Guangdong, China. <sup>3</sup>Shaoxing People's Hospital, Zhejiang University Shaoxing Hospital, Shaoxing, Zhejiang, China. <sup>4</sup>College of Animal Science and Technology, Jilin Agricultural Science and Technology College, Jilin, China. <sup>5</sup>Key Laboratory of Special Pathogens and Biosafety, Wuhan Institute of Virology, Center for Biosafety Mega-Science, Chinese Academy of Sciences, Wuhan, Hubei, China. <sup>6</sup>Zhejiang Provincial Key Laboratory of Pancreatic Disease, The First Affiliated Hospital, Institute of Translational Medicine, Zhejiang University School of Medicine, Zhejiang University, Hangzhou, China. <sup>7</sup>Zhejiang Key Laboratory of Frontier Medical Research on Cancer Metabolism, Hangzhou, China. <sup>8</sup>Department of Critical Care Medicine, Sir Run Run Shaw Hospital, Zhejiang University School of Medicine, Hangzhou, China. <sup>9</sup>Department of Physiology and Pathophysiology, School of Basic Medical Sciences, Capital Medical University, Key Laboratory of Remodeling-Related Cardiovascular Diseases, Ministry of Education, Beijing, China. <sup>10</sup>These authors contributed equally: Yanan Zhang, Shuyu Tu, Xian Shao, Jinxin Meng. ✉ e-mail: [shuzhu@zju.edu.cn](mailto:shuzhu@zju.edu.cn)

byproducts in post-damage tissue repair. Although microbial metabolites are increasingly recognized as key regulators of the ISC niche and mucosal barrier integrity<sup>7,8</sup>, the precise mechanisms bridging microbiota-derived signals to ISC behavior remain incompletely resolved. Critically, the specific commensal metabolites modulating ISC stemness, plasticity, and regenerative functions await definitive identification. Therefore, elucidating these unknown microbiota-metabolite interactions will not only reveal fundamental mechanisms governing ISC functionality but also provide actionable targets for therapeutic interventions aimed at enhancing epithelial regeneration in barrier disorders.

Integrated metabolomic profiling of IBD patients and murine colitis models revealed significant depletion of the microbiota-derived metabolite indole-3-propionic acid (IPA). We demonstrate that IPA activates peroxisome proliferator-activated receptor alpha (PPAR $\alpha$ ) through specific ligand-binding domain interactions (Tyr314/Ile317), driving 3-hydroxy-3-methylglutaryl-CoA synthetase 2 (HMGCS2)-mediated ketogenesis to elevate  $\beta$ -hydroxybutyrate (BHB) production. This metabolic cascade critically expands the LGR5<sup>+</sup> intestinal stem cell pool, thereby promoting mucosal regeneration. Furthermore, we identify *Peptostreptococcus russellii* (*P. russellii*) as an understudied commensal essential for IPA biosynthesis, establishing that tryptophan and specialized microbiota synergistically sustain IPA levels to expand the LGR5<sup>+</sup> stem cell compartment and confer potent protection against colitis.

## Results

### The abundance of IPA is decreased in human and mice with colitis

Given the well-documented alterations in microbial metabolite composition and functionality observed in inflammatory bowel disease (IBD) patients, we initiated our investigation by characterizing gut metabolic profile changes potentially associated with IBD pathogenesis. Through comparative analysis of three geographically diverse gut metabolomic datasets (four case-control comparison) encompassing IBD cohorts and non-IBD controls (including patients with varying disease activity states), we identified significant pathway enrichment in aromatic amino acid metabolism, particularly involving tyrosine, phenylalanine, and tryptophan catabolism (Fig. 1a). Among 30 conserved differential metabolites (representing 4% of total detected metabolites) across all IBD datasets (Supplementary Fig. 1a), IPA, a microbiota-derived tryptophan metabolite, demonstrated consistent depletion in IBD patients relative to non-IBD individuals, as well as in active versus quiescent disease states (Fig. 1b).

To corroborate these observational findings, we conducted quasi-targeted metabolomic profiling (covering 700 microbial metabolites) of fecal samples from 34 healthy controls and 39 Crohn's disease (CD) patients. This validation study confirmed significant downregulation of tryptophan metabolic pathways in CD patients compared to non-IBD controls (Fig. 1c), with pronounced reduction of IPA (Fig. 1d). Subsequent high-resolution LC-MS/MS quantification further validated the significantly diminished fecal IPA levels in CD patients versus healthy controls (Fig. 1e and Supplementary Fig. 1b–d).

### Microbiota-derived IPA ameliorates intestinal inflammation by restoring the mucosal barrier functions in a DSS-induced colitic mouse model

Consistent with human findings, we established a mouse model of DSS-induced colitis as previously described (Supplementary Fig. 1e–i)<sup>9</sup> and observed a progressive decrease in fecal IPA levels in DSS-treated mice (Fig. 1f). To further determine the role of IPA in the protection against IBD, groups of wild-type C57BL/6J mice (WT B6) were administered IPA through two distinct regimens according to previously published literatures: (1) daily oral gavage with 200 mg/kg or 20 mg/kg IPA for 5 days, or (2) ad libitum access to drinking water containing 200  $\mu$ g/mL

IPA for 14 days (approximately equivalent to 33 mg/kg/day), and then administered DSS for colitis induction (Supplementary Fig. 1e–ii, e–iii). Despite a gradual decline during colitis, IPA supplementation sustained significantly higher fecal levels than Veh controls throughout the entire experimental period, from baseline prior to DSS challenge and at all time points thereafter (Fig. 1f). Indeed, high-dose oral gavage (200 mg/kg) and prolonged low-dose administration via drinking water exhibited a comparable significant protective effect against DSS-induced colitis, reflected by longer colon length, alleviated histopathological changes, less infiltration of IL-6-secreting macrophages, increased number of mucin-secreting goblet cells, higher expression level of ZO-1, occluding, Muc2 and decreased colonic expression of proinflammatory cytokines IL-1 $\beta$ , IL-6 and TNF- $\alpha$  at D7 post-DSS administration (Fig. 1g–k and Supplementary Fig. 1f, g). However, low-dose IPA (20 mg/kg) administration demonstrated marginal attenuation of disease phenotypes, showing only modest mitigation in pathological indices, mucosal barrier integrity and inflammatory markers that failed to reach statistical significance compared to vehicle-treated controls (Fig. 1g–k and Supplementary Fig. 1f, g), suggesting that IPA mediates protection against DSS-induced colitis in a dose- and time course-dependent manner.

While mucosal barrier dysfunction and dysregulated T cell responses collectively drive IBD pathogenesis<sup>5,10</sup>, our assessment of IPA's immunomodulatory effects revealed no significant alterations in colonic lamina propria mononuclear cell (cLPMC) composition, including macrophages, dendritic cells, neutrophils, CD4<sup>+</sup> and CD8<sup>+</sup> T cell populations at D0 and D7 post-DSS challenge (Supplementary Fig. 1e–iv, h, i). These data suggest that IPA-mediated amelioration of intestinal injury may primarily operate through barrier restoration rather than significant modulation of these specific immune parameters at the examined time points.

### IPA exerts microbiota-independent barrier protection in colitis and extends to multiple injury models

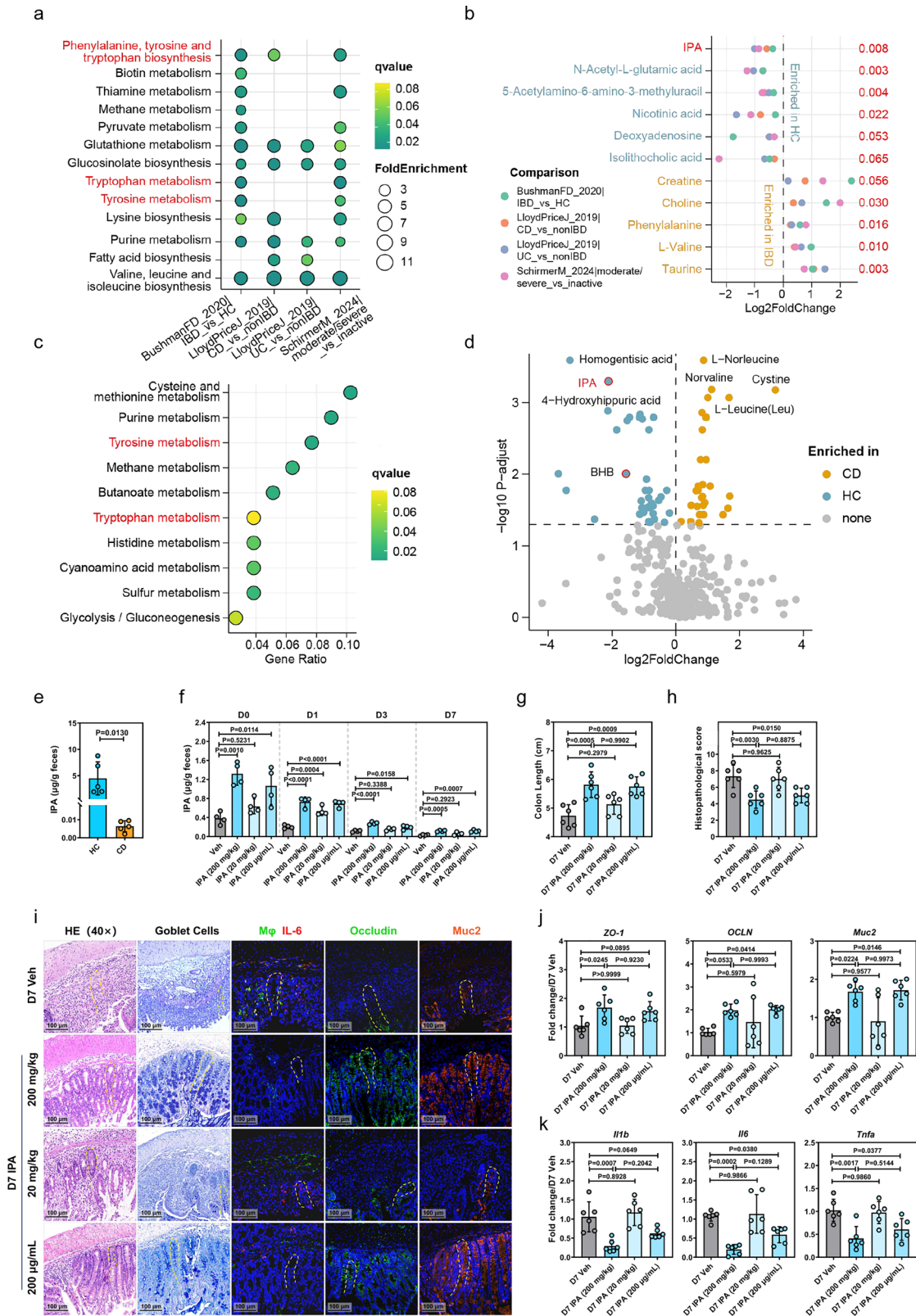
To determine whether IPA-mediated barrier protection requires microbiome involvement, GF mice were administered with IPA (GF-IPA) orally prior to DSS challenge (Supplementary Fig. 2a–i). As expected, IPA was undetectable in GF mice but elevated significantly after 5-day gavage (Supplementary Fig. 2b). Mirroring protection in conventional mice, GF-IPA attenuated colon shortening, histological damage, and pro-inflammatory cytokines while enhancing tight junctions and Muc2 expression (Fig. 2a–e; Supplementary Fig. 2c), suggesting a microbiome-independent protective function mediated by IPA supplementation.

We next extended this finding to persistent chemical injury models beyond DSS colitis. In the TNBS-induced model (Supplementary Fig. 2a–ii), IPA administration significantly mitigated disease manifestations, including attenuated colon shortening, reduced histopathological scoring, upregulated ZO-1, OCLN and Muc2 expression, and diminished *Tnfa* expression (Fig. 2f–i).

To evaluate protection against acute injury without persistent triggers, we employed a radiation enteritis (RE) model with single-dose irradiation (Supplementary Fig. 2a–iii). Consistent with chemical injury models, IPA improved ileocolonic histology, elevated tight junction proteins and Muc2, and suppressed intestinal *Tnfa* elevation at day 7 post-irradiation (Fig. 2j–m). Collectively, these results establish that IPA supplementation mitigates intestinal injury across diverse experimental models independently of microbiota modulation.

### IPA restores LGR5<sup>+</sup> ISCs and enhances epithelial regeneration in colitis by activating IEC ketogenesis

To elucidate how IPA regulates mucosal barrier function, we performed RNA-sequencing (RNA-seq) analysis of bulk colonic intestinal epithelial cells (cIECs) isolated from IPA-treated and nontreated mice



at D0, D3 and D7 post-DSS administration (Supplementary Fig. 3a). Indeed, GO and KEGG pathway enrichment analyses revealed that the upregulated differentially expressed genes resulted from IPA treatment at D7 post-DSS administration were enriched in the pathways that are important in maintaining ISC niche and mucosal barrier function, including DNA replication, cell cycle, regulation of cell division and stem cell proliferation (Fig. 3a). Significant upregulation of

aISC (*Lgr5*, *Slc12a2* and *Ascl2*) and rISC markers (*Hopx*, *Bmi1* and *Lrig1*) were observed along with increased makers of intestinal secretory linages, including Paneth cells (*Lyz1*, *Ang4* and *Agr2*), Goblet cells (*Ccl9* and *Muc2*), and Tuft cells (*Dclk1* and *Cd24a*) in the IPA-treated WT B6 mice versus Veh controls at D3 and D7 (Fig. 3b–d). However, these genes did not show obvious differences between Veh- and IPA-treated groups at D0, indicating that IPA does not significantly influence IEC

**Fig. 1 | IPA ameliorates intestinal inflammation by restoring mucosal barrier functions in a DSS-induced colitic mouse model.** **a** KEGG pathway enrichment analyses of differentially abundant metabolites across four case-control cohorts. **b** Forest plot of log<sub>2</sub> fold-change values for conserved metabolites. **c** KEGG pathway enrichment analysis of fecal metabolites differentiating Crohn's disease (CD) and healthy controls (HC). **d** The volcano plot highlights IPA enriched in HC compared to CD. **e** Fecal IPA quantification in HC/CD patients (*n* = 5). **f** Quantification of fecal IPA concentrations in C57BL/6J mice receiving either IPA or vehicle (Veh) control, before (D0) and after (days 1, 3, 7) DSS induction (*n* = 4). **g–k** IPA pretreatment (200 µg/mL drinking water for 14 d or 20/200 mg/kg gavage for 5 d) in DSS-

challenged WT mice (*n* = 6): colon length (**g**), histopathology (**h**), mucin/goblet cell markers (**i**), and *ZO-1*, *OCLN*, *Muc2*, *Il1b*, *Il6*, *Tnfa* transcripts (**j**, **k**). Functional enrichment significance was assessed using *q* values estimated by the Storey method to control the false discovery rate (**a**, **c**). A one-sided one-sample *t*-test was performed to test the directionality of enrichment relative to zero, followed by Benjamini–Hochberg (BH) correction for multiple comparisons (**b**). Data represent mean ± SD from ≥2 independent experiments, and statistical significance determined using two-sided Student's *t*-test or one-way ANOVA followed by Tukey's post hoc test for multiple comparisons (**e–h** and **j**, **k**). Source data are provided as a Source data file.

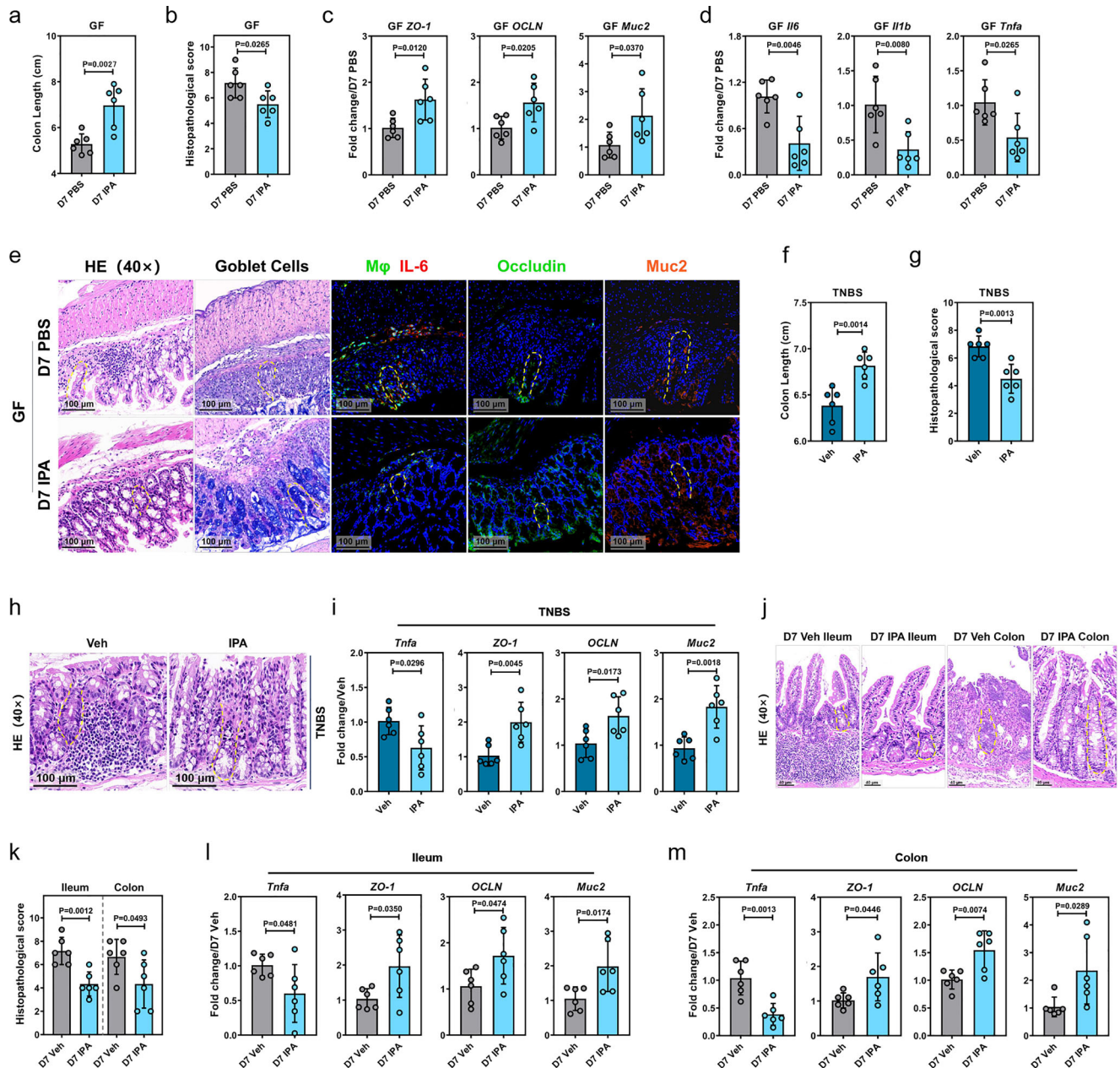
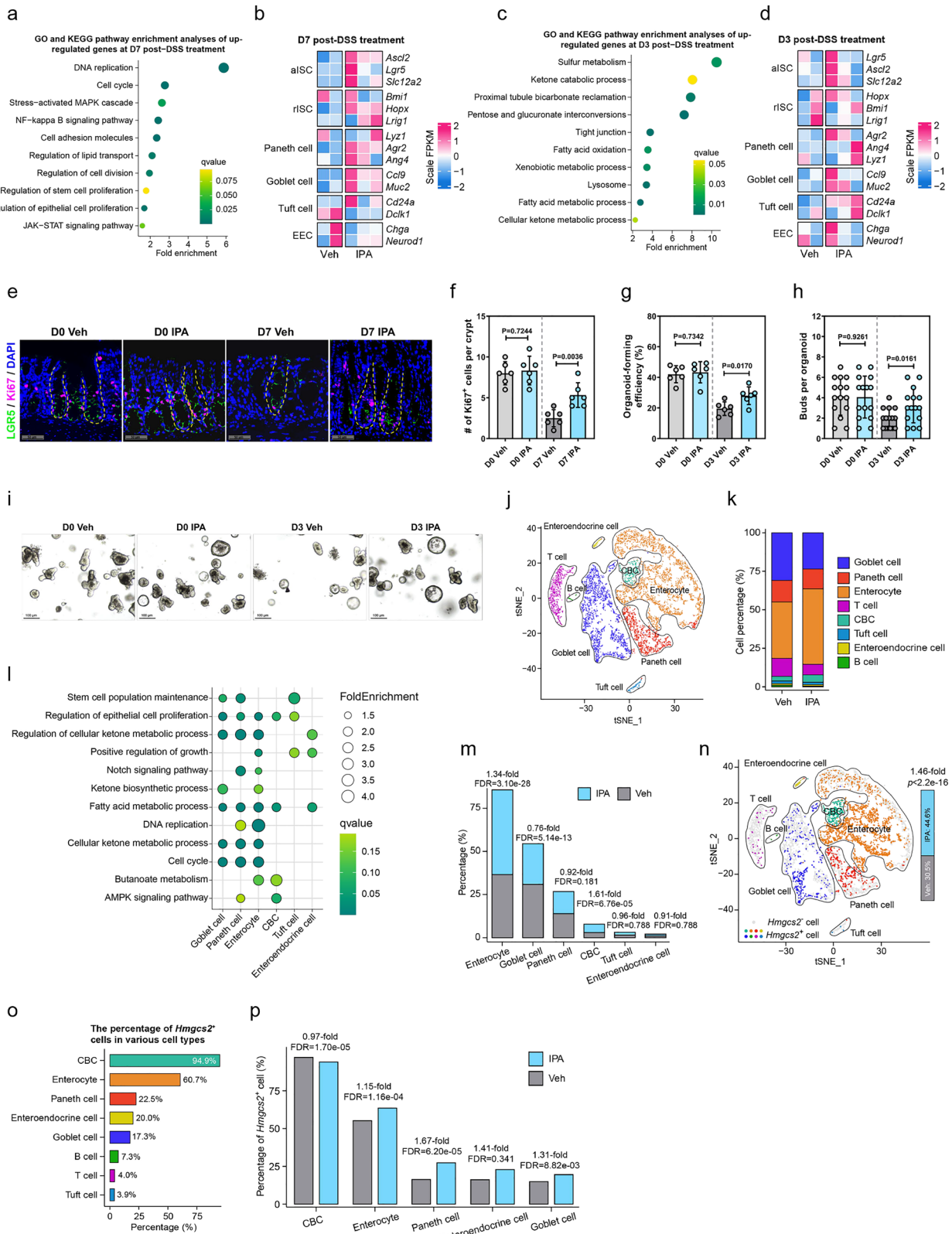


**Fig. 2 | IPA exerts microbiota-independent barrier protection in colitis and extends to multiple injury models.** **a–e** Germ-free DSS model (*n* = 6): colon length (**a**), histopathology (**b**), *ZO-1*, *OCLN*, *Muc2*, *Il1b*, *Il6* and *Tnfa* transcripts (**c**, **d**), mucin/goblet cell markers (**e**). **f–i** TNBS-colitis model (*n* = 6): colon length (**f**), histology (**g**), and HE-stained sections (**h**), and *Tnfa*, *ZO-1*, *OCLN*, *Muc2* transcripts (**i**).

**j–m** Radiation enteritis model (16 Gy IR, *n* = 6): ileal and colonic histopathology (**j**, **k**) and *Tnfa*, *ZO-1*, *OCLN*, *Muc2* gene expression (**l**, **m**). Data represent mean ± SD from ≥2 independent experiments. Statistical significance determined by two-sided Student's *t*-test. Source data are provided as a Source data file.



proliferation at homeostasis (Supplementary Fig. 3b). Consistent with the RNA-seq data, qPCR validation studies detected significantly increased expression of *Lgr5*, *Hopx*, *Muc2* and *Clu* in cIECs isolated from IPA-treated mice at D7 (Supplementary Fig. 3c). Immunofluorescent assay (IFA) of Ki67 and LGR5 further indicated a loss of LGR5<sup>+</sup> ISCs in the crypt compartments of non-treated Veh controls and restored by IPA treatment at D7 when exposed to DSS, whereas no

significant differences in immunostaining were seen between IPA- and Veh-treated mice at D0 (Fig. 3e, f).

We subsequently determined whether IPA enhances ISC proliferation in organoid assays, determining that no differences in colonic organoid formation and development were present between Veh and IPA-treated mice at D0, indicating that IPA does not affect ISC proliferation ex vivo in the absence of DSS-induced injury.

**Fig. 3 | IPA restores LGR5<sup>+</sup> ISC populations and promotes intestinal epithelium regeneration by enhancing IEC ketogenesis.** **a, c** GO and KEGG pathway enrichment analyses of upregulated genes in colonic intestinal epithelial cells (cIECs) from DSS-treated C57BL/6J mice administered 200 mg/kg IPA ( $n = 3$ ) vs. vehicle (Veh,  $n = 2$ ) at D3/D7. **b, d** Heatmaps of cell-specific marker expression in cIECs. **e** Ki67/LGR5 immunofluorescence in colon tissues from IPA/Veh-treated mice with or without DSS. **f** Ki67<sup>+</sup> cells/crypt (IFA,  $n = 6$ ). **g–i** Primary crypt cultures and crypt count at D0/D3 post-DSS; **g** Organoid-forming efficiency ( $n = 6$ ); **h** Number of buds per organoid ( $n = 15$ ); **i** Representative images. **j** t-SNE projection of 8208 single-cell transcriptomes from IPA/Veh-treated crypts. **k, m** Crypt cellular composition (stacked bars) and fold-changes in subtype percentages (IPA vs. Veh) at D3. **l** GO

and KEGG pathway enrichment analyses of differentially expressed genes across subtypes. **n–p** *Hmgcs2*<sup>+</sup> cell distribution (t-SNE), subtype percentages, and fold changes in subtype percentages (IPA vs. Veh) at D3. The accompanying bar graph in panel **n** shows the percentage of *Hmgcs2*<sup>+</sup> cells among total cells from IPA- and Veh-treated mice at D3. Functional enrichment significance was assessed using *q* values estimated by the Storey method to control the false discovery rate (**a, c, l**). Statistical significance was assessed using Fisher's exact test (**m, n**) and two-sided Wilcoxon rank-sum test (**p**), and the *P* values were adjusted for multiple testing using the BH method. Two-sided Student's *t*-tests (**f–h**) were used to assess statistical significance, and data represent mean  $\pm$  SD ( $\geq 2$  experiments). Source data are provided as a Source data file.

In comparison, colon crypts from the D3-Veh group were unable to self-expand, displayed less budding, and greater cell death and degradation, whereas crypts from IPA-treated colitic mice had superior budding and organoids forming ability (Fig. 3g–i). Together, these data suggest that IPA replenished depleted LGR5<sup>+</sup> ISCs and restored the regenerative response of the intestinal epithelium under DSS-induced colitis.

To delineate IPA's mechanism in ISC proliferation, we performed single-cell RNA sequencing (scRNA-seq) on colonic crypts from Veh- and IPA-treated mice at D3 post-DSS challenge (Fig. 3j and Supplementary Fig. 3d). IPA administration triggered substantial expansion of *Lgr5*<sup>hi</sup> ISC (CBC) and enterocyte populations, with parallel activation of butanoate metabolism-associated differentiation programs (Fig. 3k–m). Functional enrichment analyses (GO/KEGG) identified ketone body biosynthesis as the most upregulated pathway in IPA-treated goblet cells, Paneth cells, and enterocytes, constituting core modules of butanoate metabolism (Fig. 3l). This metabolic reprogramming was driven by pronounced induction of the rate-limiting enzyme HMGCS2 (1.46-fold; Fisher's exact test: odds ratio = 1.84, 95% CI = 1.67–2.02,  $p < 2.2 \times 10^{-16}$ ) (Fig. 3n), whose expression profile across colonic crypts: predominantly in CBCs (94.9%), enterocytes (60.7%), and Paneth cells (22.5%), mirrored published datasets<sup>41</sup> (Fig. 3o). Intriguingly, IPA treatment elicited a modest yet statistically significant reduction in *Hmgcs2* expression within bulk stem cell populations (0.97-fold), while simultaneously driving significant transcriptional upregulation across differentiated epithelial lineages: with enterocytes demonstrating a 1.15-fold increase, goblet cells a 1.31-fold elevation, and Paneth cells exhibiting the most pronounced amplification at 1.67-fold (Fig. 3p).

### IPA promotes LGR5<sup>+</sup> ISC proliferation in DSS-induced mice through HMGCS2

HMGCS2 is the rate-limiting enzyme in the process of ketone body production that catalyzes the synthesis of HMG-coenzyme A (CoA) from acetoacetyl-CoA and acetyl-CoA (Supplementary Fig. 4a). To elucidate the mechanistic cascade underlying IPA-induced mucosal repair, we first defined its coordinated effects on this ketogenic enzyme expression and stem cell activation. Administration of high-dose IPA (200 mg/kg, oral gavage) to WT mice significantly upregulated colonic HMGCS2 expression at D0 and D3, but not D7 post-DSS challenge compared to vehicle controls (Fig. 4a and Supplementary Fig. 4b–i, c). Concomitantly, this treatment triggered comparable *Lgr5* expression at D0 but significant upregulation at D3 and D7 post-injury (Fig. 4b). Consistent with dose dependency, both high-dose IPA via gavage (200 mg/kg) and drinking water supplementation (200  $\mu$ g/mL) robustly induced *Hmgcs2* and *Lgr5* expression at D3, whereas a lower dose (20 mg/kg gavage) yielded only non-significant or mild increasing trends for both targets (Fig. 4c, d; Supplementary Fig. 4b–ii, b–iii). These findings demonstrate that IPA may potentiate HMGCS2-mediated LGR5<sup>+</sup> ISC proliferation in dose- and time-resolved manners.

To monitor the proliferation status of ISCs after DSS-induced epithelial injury upon IPA treatment, we used *Lgr5-CreERT2*; H11-CAG-*LSL-tdTomato* mice (*Lgr5* lineage tracer, termed as *Lgr5*<sup>CreER</sup>/H11<sup>Td</sup>) for

lineage tracing (Supplementary Fig. 4b–iv). Continuous Tamoxifen (TAM) pretreatment yielded abundant tdTomato<sup>+</sup> crypt-villus clones prior to DSS administration. At this steady state (D0, 7 days after TAM treatment), IPA increased tdTomato<sup>+</sup>HMGCS2<sup>+</sup> cells per crypt but not tdTomato<sup>+</sup>Ki67<sup>+</sup> cells (Supplementary Fig. 4d–f), indicating that IPA-enhanced ketogenesis does not drive ISC proliferation under homeostasis. In contrast, upon DSS-induced injury (D3), IPA significantly elevated co-stained tdTomato<sup>+</sup>HMGCS2<sup>+</sup> and tdTomato<sup>+</sup>Ki67<sup>+</sup> cells per crypt in colonic tissues (Fig. 4e–g).

Furthermore, using a *Hmgcs2*-IEC conditional knockout (KO) mouse strain (*Villin*<sup>Cre/Cre</sup>*Hmgcs2*<sup>fl/fl</sup>, termed as *Hmgcs2*<sup>ΔIEC</sup>) (Supplementary Fig. 4b–v), we determined HMGCS2 essentially by showing that IPA boosted *Lgr5* expression at D3 and crypt Ki67<sup>+</sup> cells at D7 post-injury in *Hmgcs2*<sup>fl/fl</sup> littermate Veh controls, whereas this effect was abolished in *Hmgcs2*<sup>ΔIEC</sup> mice (Fig. 4h–j). Collectively, these results definitively demonstrate that IPA stimulates post-injury expansion of the LGR5<sup>+</sup> ISC pool through HMGCS2.

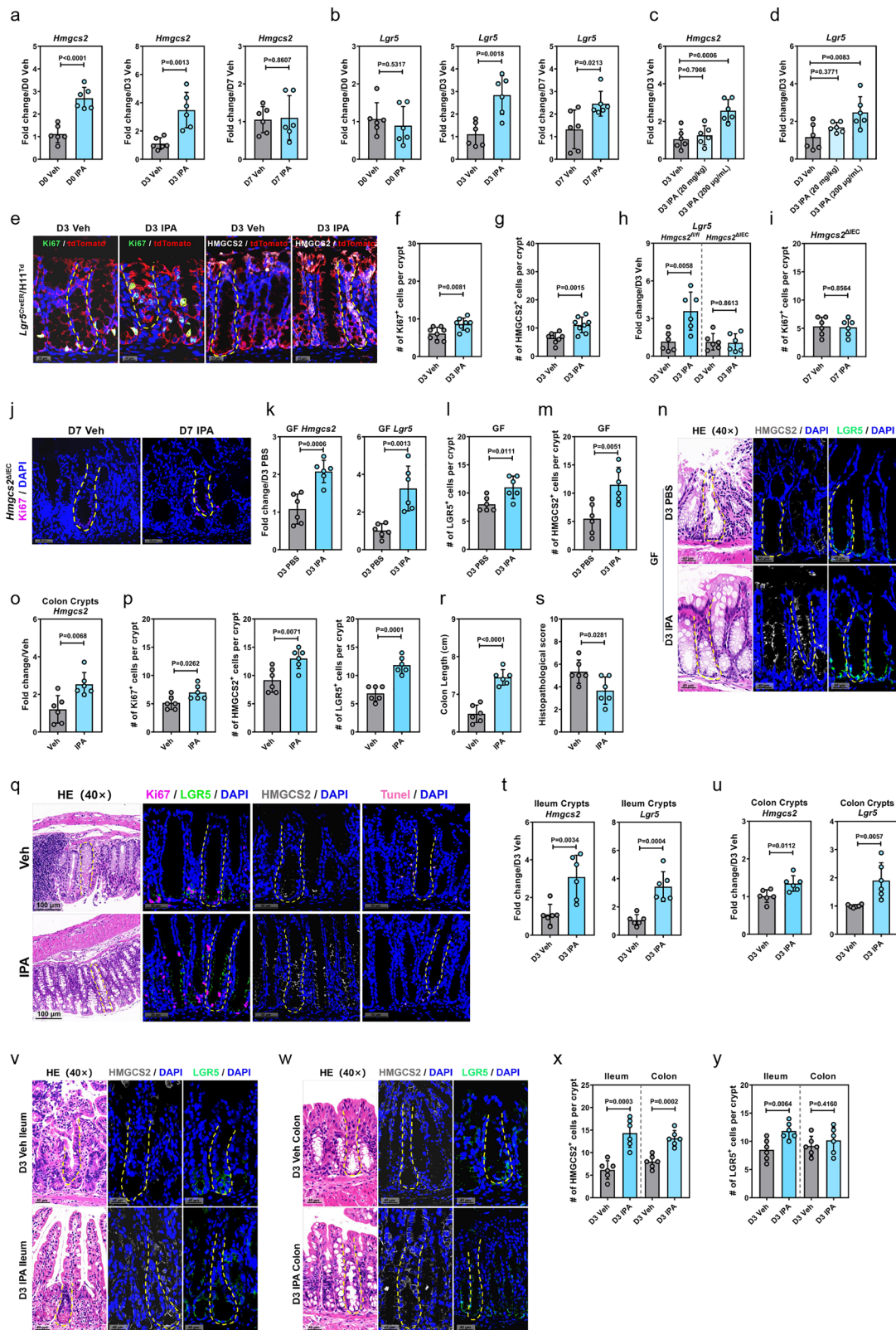
### IPA potentiates microbiota-independent LGR5<sup>+</sup> ISC proliferation with expanded efficacy across injury models

To verify that IPA induces HMGCS2 upregulation through microbiota-independent mechanisms, we performed parallel IPA protective experiments in GF mice (Supplementary Fig. 4b–vi). Expectedly, IPA-treated GF mice showed markedly increased HMGCS2 and LGR5 expression in colonic tissues at D3 post-DSS challenge compared to PBS controls both by qPCR and IFA (Fig. 4k–n).

To directly illustrate the enhancing effect exerted by IPA on LGR5<sup>+</sup> ISC proliferation during the regenerative process, WT B6 mice were gavaged with IPA post-DSS withdrawal (Supplementary Fig. 4b–vii). Colon tissues analyzed at day 5 post-IPA treatment (allowing ~ two renewal cycles, as the epithelium renews itself every 3–5 days) revealed markedly enhanced *Hmgcs2* expression, HMGCS2<sup>+</sup> signals and LGR5<sup>+</sup>Ki67<sup>+</sup> ISCs in IPA-treated versus Veh controls (Fig. 4o–q). Concomitantly, IPA-treated mice showed significant improvements in colon length, histopathological scores, and apoptotic cell reduction (Fig. 4r, s).

To further evaluate the relevance of IPA in a context mimicking chronic relapsing inflammation, we extended the recovery-phase analysis to 2–3 weeks post DSS treatment (covering 4–6 epithelial renewal cycles) in WT B6 mice (Supplementary Fig. 4b–viii). These long-term observations confirmed that the regenerative benefits of IPA, including sustained elevation of *Hmgcs2* and enhanced LGR5<sup>+</sup> ISC activity at D17 post-DSS (Supplementary Fig. 4g–i), while *Hmgcs2* mRNA levels showed no significant difference between IPA and Veh groups, HMGCS2<sup>+</sup> signals remained slightly elevated without reaching statistical significance at D22 after DSS induction (Supplementary Fig. 4g, h). Nevertheless, IPA-treated mice continued to exhibit sustained improvements in colon length and histopathological scores (Supplementary Fig. 4j, k), indicating a durable protective effect in prolonged recovery.

Extending these observations to the RE mouse model, IPA-pretreated mice exhibited robust induction of ileocolonic *Hmgcs2* and *Lgr5* expression at D3 after 16 Gy abdominal IR (Fig. 4t–y and Supplementary Fig. 4b–ix). Taken together, these data demonstrate that IPA accelerates mucosal repair across barrier injury models by



potently stimulating LGR5<sup>+</sup> ISC proliferation and HMGC2-mediated ketogenesis, thus promoting epithelial regeneration.

**IPA-driven BHB production via enhanced ketogenesis compensates for LGR5<sup>+</sup> ISC depletion in colitis**

Given that HMGC2 serves as the rate-limiting enzyme for ketogenesis and is potently induced by IPA, we next quantified BHB kinetics in

colonic IECs from IPA- and vehicle-treated mice. BHB levels were significantly elevated at D0, D1, and D3 post-DSS in IPA-treated animals, though with a progressive decline over time (Fig. 5a and Supplementary Fig. 5a-i). This temporal profile mirrored *Hmgs2* and *Lgr5* expression patterns in IECs (Fig. 4a, b).

Complementarily, serum BHB increased in IPA-treated mice prior to DSS exposure, whereas hepatic BHB remained unchanged

**Fig. 4 | IPA promotes LGR5<sup>+</sup> ISC proliferation in DSS-induced mice via HMGS2 in IECs.** **a, b** Temporal *Hmgcs2* (**a**) and *Lgr5* (**b**) expression in colonic crypts of WT mice treated with 200 mg/kg IPA post-DSS ( $n = 6$ ). **c, d** *Hmgcs2* and *Lgr5* expression (qRT-PCR) in crypts of WT mice treated with IPA (200  $\mu$ g/mL water for 14 d or 20 mg/kg gavage for 5 d) at D3 post-DSS ( $n = 6$ ). **e–g** Lineage tracing in *Lgr5*<sup>CreER</sup>/H11<sup>Td</sup> mice: **e** Co-staining for Ki67/HMGS2; **f, g** Quantification of Ki67<sup>+</sup> and HMGS2<sup>+</sup> cells/crypt (IFA,  $n = 8$ ). **h** *Lgr5* expression in *Hmgcs2*<sup>fl/fl</sup> and *Hmgcs2* <sup>$\Delta$ IEC</sup> mice crypts at D3 post-DSS ( $n = 6$ ). **i, j** Ki67 in *Hmgcs2* <sup>$\Delta$ IEC</sup> crypts ( $n = 6$ ). **k–n** Colonic

HMGS2/LGR5 expression in GF mice (**k**: qRT-PCR; **l–n**: IFA;  $n = 6$ ). **o–s** Therapeutic IPA (200 mg/kg for 5d) post-DSS ( $n = 6$ ): **o** *Hmgcs2* expression (qRT-PCR); **p, q** Regenerative crypt markers (Ki67/LGR5/HMGS2/TUNEL) post-DSS recovery; **r, s** Colon length and histopathology. **t–y** Ileal and colonic HMGS2/LGR5 expression in RE model (16 Gy IR,  $n = 6$ ): (**t, u**: qRT-PCR; **v–y**: IFA). Data represent mean  $\pm$  SD from  $\geq 2$  independent experiments. Statistical significance determined by two-sided Student's *t*-test or one-way ANOVA followed by Tukey's post hoc test for multiple comparisons. Source data are provided as a Source data file.

(Supplementary Fig. 5b, c). Consistently, *Hmgcs2* upregulation was restricted to colonic crypts with no induction in liver tissue at D3 (Supplementary Fig. 5d), indicating that IECs rather than hepatic cells are the most likely cellular source of endogenous BHB enhancement attributed to IPA administration.

It has been demonstrated that endogenous BHB produced by HMGS2-mediated ketogenesis in LGR5<sup>+</sup> ISCs regulates stemness and proliferation through Notch signaling under homeostasis<sup>12</sup>. Thus, we postulated that BHB treatment might similarly triggered a significant, time-dependent expansion of the LGR5<sup>+</sup> ISC compartment like IPA does. Indeed, BHB pretreatment recapitulated the temporal expression patterns of *Lgr5* observed with IPA administration (Fig. 5b and Supplementary Fig. 5a-ii). Moreover, Immunofluorescence analysis (IFA) of DSS-challenged WT-Veh mice revealed early-phase (D3) depletion of LGR5<sup>+</sup> ISCs, reflecting rapid mucosal repair mechanisms (Fig. 5c, d). By D7 post-injury, these controls exhibited severe crypt atrophy with diminished LGR5 expression and impaired proliferative capacity, consistent with prior reports<sup>13</sup>. In contrast, both WT-IPA and WT-BHB groups demonstrated sustained amplification of LGR5<sup>+</sup> ISCs at D3 and D7 (Fig. 5c, d).

This enhancement of LGR5<sup>+</sup> aISCs was further corroborated in the RE injury model, where ileal/colonic crypts from treated mice displayed robust upregulation of *Lgr5* transcripts at D3 post-IR (Fig. 5e–g and Supplementary Fig. 5a-iii, e). These protective effects extended to the D7 IR model, where BHB significantly ameliorated pathological manifestations through improved histoarchitectural preservation, enhanced barrier integrity, and suppressed inflammatory cytokine *Tnfa* (Fig. 5h–j and Supplementary Fig. 5f).

Since BHB has been reported to inhibit the NLRP3 inflammasome<sup>14</sup>, groups of WT B6 and *Nlrp3*<sup>-/-</sup> mice were administered IPA or BHB before DSS exposure (Supplementary Fig. 5a-iv, v). Significantly elevated *Lgr5* mRNA levels were observed regardless of the host genotype (Fig. 5k), indicating that the BHB-driven reconstitution of LGR5<sup>+</sup> ISCs after injury was independent of the NLRP3 inflammasome.

### IPA and BHB restore LGR<sup>+</sup> ISC proliferation in both murine and human organoids

Building upon our in vivo observations that IPA enhances HMGS2-mediated ketogenesis and expands the LGR5<sup>+</sup> ISC compartment in both conventional and GF mice, we next assessed whether IPA acts intrinsically within IECs to induce this pathway. Treating colonic organoids derived from GF mice with IPA resulted in a dose-dependent upregulation of *Hmgcs2* expression and a concomitant increase in BHB concentration in the culture supernatant (Fig. 5l, m and Supplementary Fig. 5g-i). Extending this to an inflammatory context, GF-derived organoids pretreated with IPA or BHB prior to TNF $\alpha$ /IFN $\gamma$  exposure (stimulation; ST) exhibited significantly elevated *Lgr5* transcript levels at 18 h post-injury (Fig. 5n and Supplementary Fig. 5g-ii, iii).

Critically, this pathway is conserved in human systems. IPA similarly induced HMGS2 expression and BHB production in human colonic organoids (Fig. 5o–q; Supplementary Fig. 5g-iv). Upon proinflammatory cytokine challenge, IPA or BHB pretreatment triggered a biphasic stemness response. This response manifested as transient suppression of baseline LGR5 (0 h) followed by robust amplification

during regeneration (24–48 h) (Fig. 5r–t and Supplementary Fig. 5g-v, vi).

Concurrently at 48 hpt, we observed a pro-regenerative molecular signature featuring coordinated induction of Notch/Wnt effectors (*HES1*, *CTNNB1*) alongside epithelial differentiation markers (*LYZ*, *MUC2*), while key inflammatory cytokines (*IL1B*, *IL8*, *TNFA*) were significantly downregulated (Fig. 5u, v).

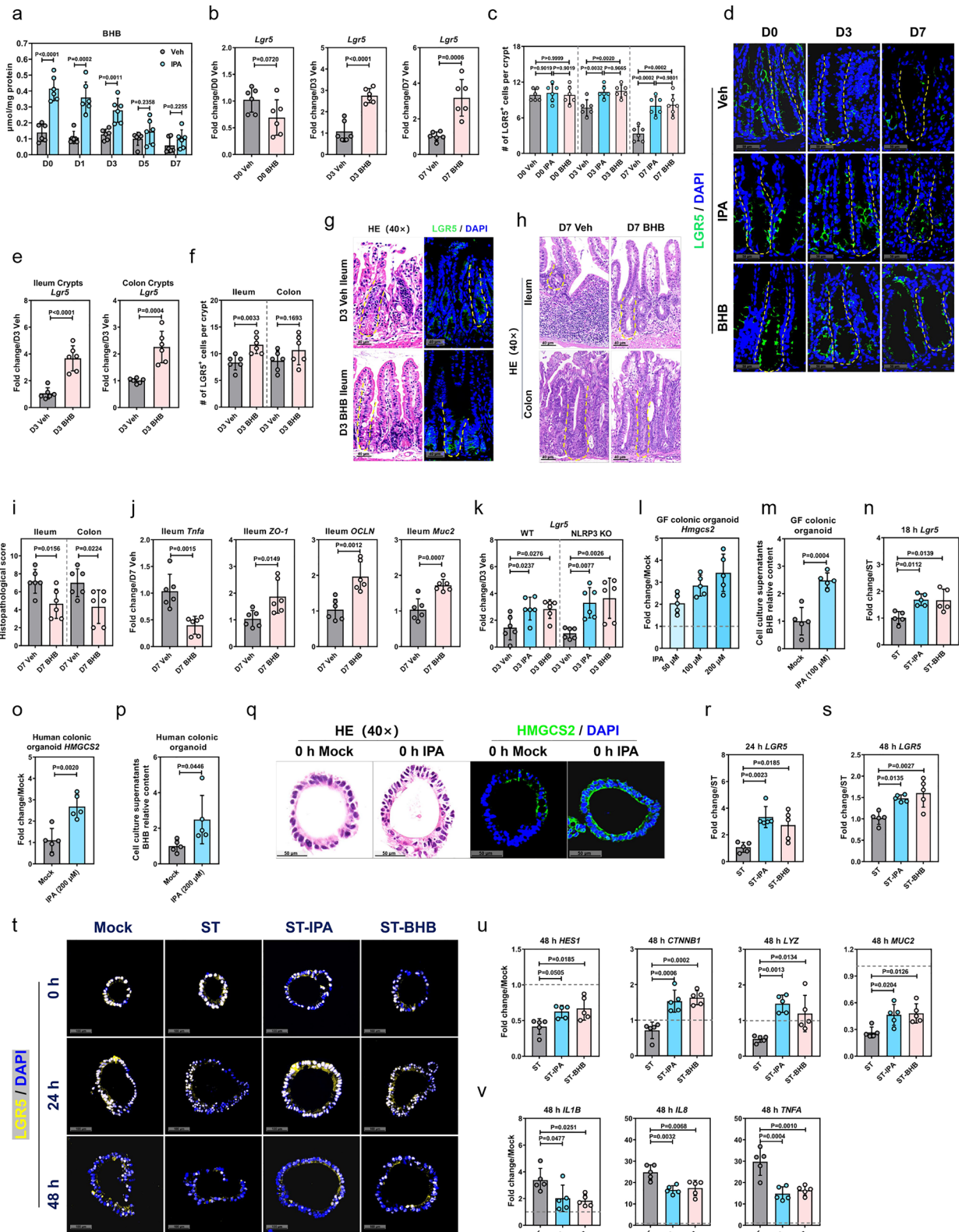
### IPA promotes HMGS2-mediated ketogenesis of LGR5<sup>+</sup> ISCs through PPAR $\alpha$

Complementing the predominant enrichment of ketone catabolic processes, our bulk RNA-seq analysis identified concurrent upregulation of fatty acid metabolism and oxidation among differentially expressed genes in cIECs from IPA-treated mice at D3 post-DSS challenge (Fig. 3c). The PPAR family is composed of three members, PPAR $\alpha$ , PPAR $\beta/\delta$  and PPAR $\gamma$ . Accumulating evidence has demonstrated that PPAR $\alpha$  is a key element in the metabolic network of fatty acid oxidation (FAO) and ketogenesis that induces endogenous HMGS2 expression<sup>15–17</sup>. Although not as robust as the selective PPAR $\alpha$  agonist WY14643, IPA markedly increased *HMGS2* expression in human colonic organoids by almost 4-fold, while the enhancing effect was greatly neutralized by treatment with the PPAR $\alpha$  antagonist MK886 (Fig. 6a-i, b).

To corroborate that IPA promotes HMGS2-mediated ketogenesis through PPAR $\alpha$  activation, we introduced a PPAR $\alpha$  IEC-specific knockout mouse line (*Villin*<sup>cre/cre</sup>*Ppara*<sup>fl/fl</sup>, termed as *Ppara* <sup>$\Delta$ IEC</sup>) and performed the organoid assays (Fig. 6a-ii). As expected, the IPA-mediated upregulation of *Hmgcs2* expression was significantly blunted by MK886 in colonic organoids from *Ppara*<sup>fl/fl</sup> littermates, whereas this difference was not seen in the colonic organoids collected from *Ppara* <sup>$\Delta$ IEC</sup> mice (Fig. 6c, d). In line with this observation, hindering PPAR $\alpha$  activity resulted in a significant reduction in IPA-mediated augmentation of BHB production (Fig. 6e). *Ppara* <sup>$\Delta$ IEC</sup> colonic organoids pretreated with IPA prior to inflammatory injury induction exhibited no differences in modulating *Lgr5* expression at 18 hpt (Fig. 6a-iii, f). These data suggested that IPA enhances HMGS2-mediated ketone body metabolism via PPAR $\alpha$  under both homeostatic and injury conditions ex vivo.

To evaluate the effects of IPA on PPAR $\alpha$  activation in vivo, groups of *Ppara* <sup>$\Delta$ IEC</sup> mice were treated with IPA prior to DSS administration (Fig. 6a-iv). Consistent with the ex vivo organoid assays, IPA administration to *Ppara* <sup>$\Delta$ IEC</sup> mice significantly increased the IPA concentration in the colon tissues but failed to boost *Hmgcs2* and *Lgr5* expression at D3 at either the transcriptional or translational level in the colon crypts, and did not enhance BHB production (Fig. 6g, h), which was similar to the results of experiments using *Hmgcs2* <sup>$\Delta$ IEC</sup> mice (Fig. 4h–j).

Since IPA has been reported to ameliorate various immune-related diseases through the aryl hydrocarbon receptor (AhR)<sup>18–20</sup>, and given emerging evidence that it also enhances intestinal barrier integrity and alleviated IBD as well as radiation-induced intestinal injury via the pregnane X receptor (PXR)<sup>21–23</sup>, we administered IPA to a mouse line with *Ahr* conditional knockout in IECs (*Villin*<sup>cre/cre</sup>*Ahr*<sup>fl/fl</sup>, termed as *Ahr* <sup>$\Delta$ IEC</sup>) and similarly to *Pxr*<sup>-/-</sup> mice, followed by DSS-induced colitis (Fig. 6a-v, vi). At D3 post-DSS administration, IPA treatment significantly upregulated *Hmgcs2* and *Lgr5* in both *Ahr* <sup>$\Delta$ IEC</sup> and *Pxr*<sup>-/-</sup> mice (Fig. 6i, j), comparable to the effects observed in WT B6 mice,



indicating that the IPA phenotype is independent of both AhR and PXR signaling.

Furthermore, there were no differences in disease phenotype, histological changes, mucosal barrier function (however, IPA treatment led to elevated *Muc2* expression) and proinflammatory cytokine expression at D7 post-DSS administration between IPA-treated and nontreated *Ppara*<sup>ΔIEC</sup> mice (Fig. 6k, l). Taken together, these results

suggest that IPA may accelerate the *LGR5*<sup>+</sup> ISC proliferation through a PPARα-HMGS2-BHB axis.

**IPA binds the ligand-binding domain of PPARα to promote its activity on transcriptional regulation**

The PPAR family members are ligand-activated transcriptional regulators that bind to PPAR response elements (PPREs) to initiate gene

**Fig. 5 | BHB produced via IPA-enhanced ketogenesis rescues LGR5<sup>+</sup> ISC depletion.** **a** Temporal  $\beta$ -hydroxybutyrate (BHB) levels in cIECs post-DSS ( $n = 6$ ). **b** Kinetics of *Lgr5* expression in BHB-treated (40 mg/25 g) WT mice post-DSS ( $n = 6$ ). **c, d** Quantification of LGR5<sup>+</sup> cells/ crypt (IFA) in DSS model ( $n = 6$ ). **e–j** RE model analysis (16 Gy IR,  $n = 6$ ): **e** *Lgr5* (qRT-PCR); **f, g** LGR5 (IFA); **h, i** Histopathology (HE); **j** *Tnfa*, *ZO-1*, *OCLN* and *Muc2* expression in ileum. **k** *Lgr5* expression (qRT-PCR) in WT/*Nlrp3*<sup>-/-</sup> mice at D3 post-DSS ( $n = 6$ ). **l, m** *Hmgcs2*/BHB levels in germ-free organoids  $\pm$  IPA ( $n = 5$ ). **n** *Lgr5* expression (qRT-PCR) in germ-free organoids  $\pm$  IPA/

BHB ( $n = 5$ ). **o, q** *HMGCS2* expression/IFA in human organoids ( $n = 5$ ). **p** BHB in human organoid supernatants post-IPA (200  $\mu$ M, 6 h;  $n = 5$ ). **r–t** LGR5 dynamics in human organoids post-cytokine injury with or without IPA/BHB pretreatment ( $n = 5$ ). **u, v** qRT-PCR analyses of *IL1B*, *IL8*, *TNFA*, *HES1*, *CTNNB1*, *LYZ* and *MUC2* in human organoids at 48 h post-injury ( $n = 5$ ). Data represent mean  $\pm$  SD from  $\geq 2$  independent experiments. Statistical significance determined by two-sided Student's t-test or one-way ANOVA followed by Tukey's post hoc test for multiple comparisons. Source data are provided as a Source data file.

transcription<sup>24</sup>. We hypothesized that IPA promotes HMGCS2-mediated ketogenesis by driving PPAR-dependent *Hmgcs2* transcription. To test this idea, we first searched for PPRES in the *Hmgcs2* promoter, finding a canonical PPRES in its 5' upstream region (Fig. 7a). Notably, by reporter analysis, the PPRES-binding activity of the PPAR $\alpha$  ligand-binding domain (LBD), but not the LBDs of the other two isoforms, was specifically enhanced by IPA in a dose-dependent manner (Fig. 7b). Hence, colon crypts isolated from *Ppara*<sup>fl/fl</sup> mice treated with IPA had significantly increased binding of PPAR $\alpha$  to PPRES as determined by ChIP-qPCR, approximately 3.5-fold greater than those from nontreated controls, but this difference was not seen between treated and nontreated colon crypts from *Ppara*<sup>ΔIEC</sup> mice (Fig. 7c).

We analyzed our scRNA-seq datasets and found that IPA administration did not upregulate overall *Ppara* expression in the colonic crypts at D3 post-DSS administration (Fig. 7d). Also, qPCR failed to detect changes in the expression of any of the three PPAR isoforms in the colon or ileum crypts of IPA-treated animals, in either the DSS or IR injury models (Fig. 7e, f). Based on these results, we hypothesized that the IPA might directly interact with PPAR $\alpha$  to enhance downstream *Hmgcs2* expression and ketone body production. Thus, we synthesized biotinylated IPA (biotin-IPA) and mixed it with whole-cell extracts from human and mouse colonic organoids. In vitro pull-down assays demonstrated that IPA directly bound to both human and mouse PPAR $\alpha$  (Fig. 7g, h). Subsequently, biotin-IPA pull-down assays with 293 T cells transfected with a PPAR $\alpha$  LBD construct suggested that IPA may bind to the LBD, which is essential for the PPAR $\alpha$ -ligand interaction (Fig. 7i)<sup>24</sup>.

We further investigated the interaction between IPA and PPAR $\alpha$  LBD through molecular docking analysis. The interaction distances between certain amino acids residues (Thr279, Ser280, Tyr314, Ile317, Phe318, Ile354, Met355, and His440) and IPA were less than 5 Å, and these amino acids residues were chosen for subsequent functional investigation (Fig. 7j). We discovered that mutating Tyr314 or Ile317 to alanine (A) completely abolished the IPA-mediated enhancement of PPAR $\alpha$  LBD's binding activity to the PPRES, as assessed by reporter gene analysis (Fig. 7k). Additionally, mutation of Tyr314 to phenylalanine (F) or valine (V), and Ile317 to aspartic acid (D), resulted in a partial loss of the IPA-induced enhancement of PPAR $\alpha$  LBD's PPRES-binding capacity (Fig. 7l). Conversely, MelAA, an unrelated indole derivative used as a control, did not clearly stimulate the PPRES-binding activity of PPAR $\alpha$  LBD (Fig. 7l).

Supporting our findings from the luciferase assay, we utilized a Cellular Thermal Shift Assay (CETSA) to evaluate the impact of IPA on the protein stability of PPAR $\alpha$  LBD, demonstrating that IPA significantly bolsters its thermostability, an effect that is markedly attenuated by mutation of Tyr314 or Ile317 to Alanine (Fig. 7m, n). These data indicate that IPA enhances the binding of the PPAR $\alpha$  LBD to the PPRES through a direct interaction with the critical amino acid residues Tyr314 and Ile317, and subsequent enhancement of *Hmgcs2* transcription.

### ***P. russellii* produces IPA and improves HMGCS2-mediated LGR5<sup>+</sup> ISC proliferation**

Trp can be sequentially catabolized by commensal bacteria into indole-3-pyruvic acid (IPYA), indole-3-lactic acid (ILA), indole-3-acrylic

acid (IA), and indole-3-propionic acid (IPA)<sup>26</sup> (Supplementary Fig. 6a). Among these indole derivatives, IPA production has been most extensively characterized in the bacterial strain *Clostridium sporogenes* (*C. sporogenes*)<sup>26,27</sup>. Additionally, a limited number of *Peptostreptococcus* species, including *Peptostreptococcus anaerobius* (*P. anaerobius*) and *Peptostreptococcus russellii* (*P. russellii*), have been identified as efficient IPA producers<sup>28,29</sup>.

Building on the functional evidence of IPA's role in enhancing ISC activity in both human organoid and mouse colitic models, we sought to explore the clinical relevance of IPA-producing bacteria and IPA levels in human IBD patients. By reanalyzing stool metagenomic datasets from geographically distinct IBD cohorts, we identified a significant enrichment of *P. russellii* in fecal samples from healthy controls compared to those from UC and CD patients (Fig. 8a–d). Moreover, linear correlation analysis within our CD cohort revealed a direct relationship between reduced *P. russellii* abundance and lower IPA concentrations in these patients (Fig. 8e).

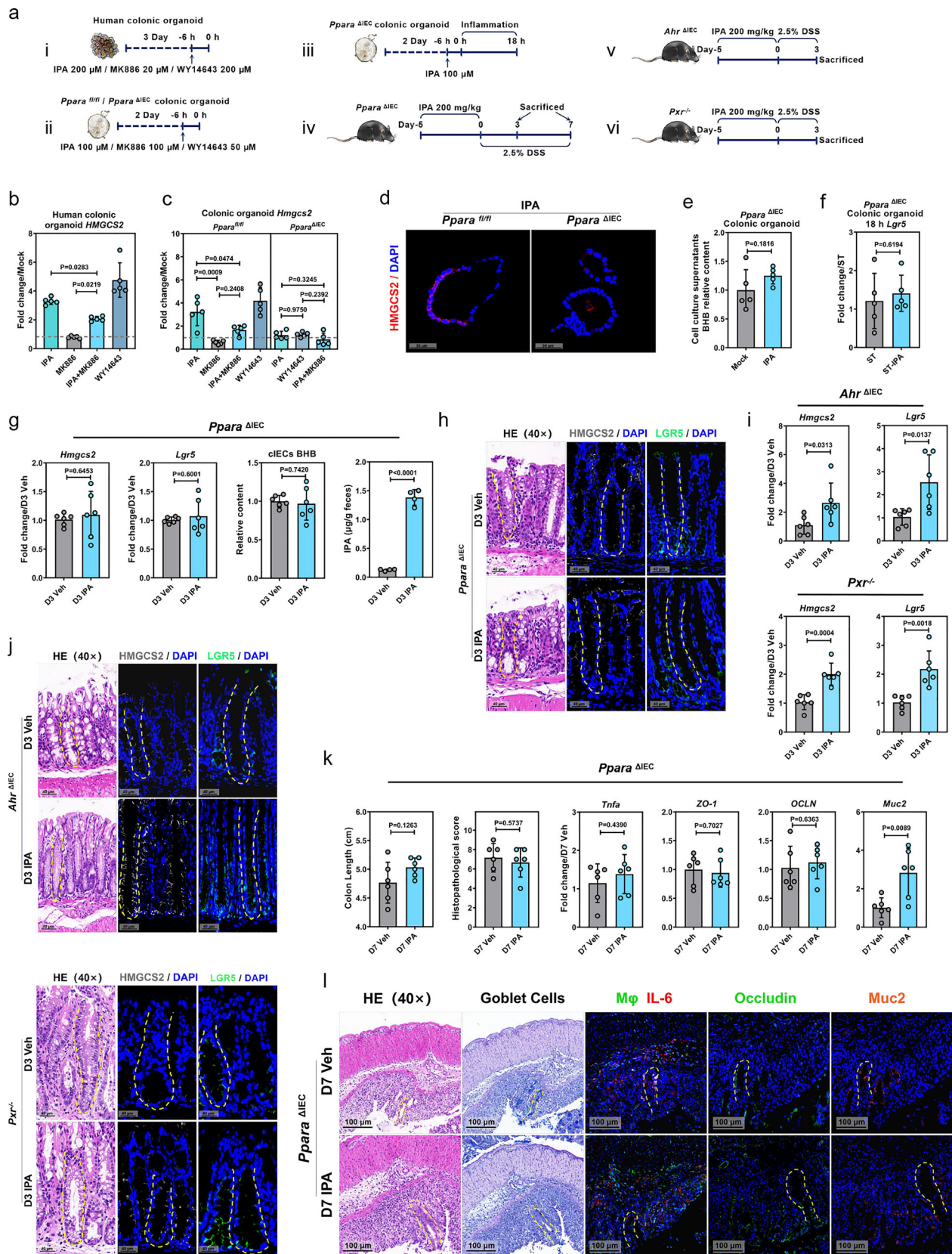
To validate the IPA-producing capacity of *P. russellii* through Trp degradation in vitro, we supplemented the culture medium with Trp and observed a clear dose-dependent accumulation of IPA in the supernatants of both *P. russellii* and *C. sporogenes* (served as positive control) (Fig. 8f and Supplementary Fig. 6b).

Given *P. russellii*'s demonstrated high in vitro IPA production capacity, we hypothesized that its colonization might compensate for LGR5<sup>+</sup> ISC depletion by activating HMGCS2-dependent ketogenesis to drive epithelial repair in DSS-induced colitis. Pre-DSS colonization indeed restored fecal IPA levels in *Hmgcs2*<sup>ΔIEC</sup> mice (Supplementary Fig. 6c–i, d). At D3 post-treatment, *P. russellii* colonization induced coordinated upregulation of *Lgr5* in *Hmgcs2*<sup>fl/fl</sup> but not *Hmgcs2*<sup>ΔIEC</sup> littermates (Fig. 8g).

To evaluate *P. russellii*'s colitis-protective capacity in GF settings, we compared DSS-challenged GF mice colonized with *P. russellii* versus those receiving WT B6 FMT (Supplementary Fig. 6c–ii). *P. russellii*-monocolonized mice exhibited superior colonization efficiency versus FMT controls (Supplementary Fig. 6e), accompanied by elevated fecal/serum IPA levels confirming microbial-specific metabolite production (Fig. 8h, i). At D3 post-DSS, these mice demonstrated upregulated *Hmgcs2* and *Lgr5* expression compared to FMT counterparts (Fig. 8j–l), progressing to D7 phenotypic improvements including attenuated colon shortening, reduced histopathology, enhanced barrier integrity, and suppressed inflammation (Fig. 8m–q). These findings establish *P. russellii* as a microbial orchestrator of HMGCS2-mediated ketogenesis, driving LGR5<sup>+</sup> ISC proliferation and mucosal repair in vivo.

## **Discussion**

Dysregulation of ISCs compromises epithelial barrier function and directly affects the development and pathogenesis of intestinal diseases. Emerging evidence points towards the gut microorganisms and their metabolic products as critical factors in inducing epithelium regeneration post-intestinal damage. However, the role of specific microbial metabolites and the underlying mechanisms of ISC-associated tissue repair remained mostly elusive. Here we describe that microbiota-derived IPA plays a pivotal role in intestinal epithelium regeneration by restoring LGR5<sup>+</sup> ISC populations through HMGCS2-



mediated ketogenesis in IECs (Fig. 8r). Our work builds on the limited understanding of the conserved commensal bacteria-host metabolic interaction of vital importance both in physiological conditions as well as disease settings in IBD and RE, and potentially, other intestinal disorders with epithelium damages.

While IPA administration significantly attenuated DSS-induced colitis through reduced inflammation and enhanced barrier repair, our flow cytometric analysis revealed no overt alterations in major colonic immune populations (macrophages, dendritic cells, neutrophils, CD4<sup>+</sup>/CD8<sup>+</sup> T cells) at D0 or D7 post-injury (Supplementary Fig. 1i).

**Fig. 6 | IPA promotes HMGCS2-mediated ketogenesis of LGR5<sup>+</sup> ISCs through PPAR $\alpha$ .**

**a** Experimental schematics: (i–iii) Human/murine organoid treatments with IPA (100–200  $\mu$ M), MK886 (20–100  $\mu$ M), or WY14643 (50–200  $\mu$ M); (iv–vi) IPA and DSS administration in *Ppara*<sup>ΔIEC</sup>/*Ahr*<sup>ΔIEC</sup>/*Pxr*<sup>-/-</sup> mice. **b, c** *Hmgcs2/Hmgcs2* expression in human (**b**  $n = 5$ ) or *Ppara*<sup>fl/fl</sup>/*Ppara*<sup>ΔIEC</sup> (**c**  $n = 5$ ) murine organoids with or without pharmacological modulators. **d** HMGCS2 immunofluorescence in *Ppara*<sup>fl/fl</sup> or *Ppara*<sup>ΔIEC</sup> organoids with IPA treatments. **e** BHB levels in *Ppara*<sup>ΔIEC</sup> organoid supernatants with IPA ( $n = 5$ ). **f** *Lgr5* expression in cytokine-challenged *Ppara*<sup>ΔIEC</sup> organoids with IPA at 18 h post injury ( $n = 5$ ).

**g** *Hmgcs2/Lgr5* expression ( $n = 6$ ), BHB ( $n = 6$ ) and IPA ( $n = 4$ ) levels in DSS-challenged *Ppara*<sup>ΔIEC</sup> mice with IPA. **h–j** HMGCS2/LGR5 expression in *Ppara*<sup>ΔIEC</sup> (**h**), *Ahr*<sup>ΔIEC</sup> and *Pxr*<sup>-/-</sup> mice (**i**, qPCR,  $n = 6$ ; **j**, IFA). **k, l** Phenotypic analyses of DSS-challenged *Ppara*<sup>ΔIEC</sup> mice plus IPA ( $n = 6$ ): colon length, histopathology, *Tnfa/ZO-1/OCLN/Muc2* (**k**); mucin/goblet cell markers (**l**). Data represent mean  $\pm$  SD from  $\geq 2$  independent experiments. Statistical significance determined by two-sided Student's t-test or one-way ANOVA followed by Tukey's post hoc test for multiple comparisons. Source data are provided as a Source data file.

These observations differ contextually from established roles of IPA in suppressing Th1/Th17 responses via HSP70-mediated apoptosis<sup>30</sup> or augmenting CD8<sup>+</sup> T cell stemness for pan-cancer immunotherapy<sup>30</sup>. We posit this divergence arises from distinct disease models (acute epithelial injury vs chronic colitis/cancer systems), our broad immune profiling which lacked resolution for specific T-cell subsets, or differing kinetic windows of analysis.

While the role of HMGCS2 in promoting the stemness of small intestinal LGR5<sup>+</sup> ISCs through BHB production is recognized under normal physiological conditions<sup>12</sup>, the specific microbiota-derived signals that modulate synthesis of this ketone body in ISCs in response to mucosal injury remain largely undefined. Employing scRNA-seq, lineage tracing, and conditional ablation, our research uncovers a regulatory mechanism wherein IPA enhances HMGCS2-dependent ketogenesis in IECs to restore LGR5<sup>+</sup> ISC pool and significantly contribute to epithelial regeneration in DSS-induced colitis and RE mouse models (Figs. 3n–p and 4e–j).

Profiling of colon crypts derived from IPA-treated mice prior to DSS exposure demonstrated an upregulation of *Hmgcs2* and genes associated with ketogenesis accompanied by heightened BHB production and unaffected *Lgr5* levels (Fig. 5a–d). These data are consistent with the research conducted by Oxana et al. using mouse models of colorectal cancer (CRC), in which ketogenic diets and BHB were reported to reduce the proliferation of colonic crypt cells and potentially suppress intestinal tumor growth through HOPX<sup>31</sup>. Here, we demonstrate that IPA-driven HMGCS2-mediated BHB synthesis in IECs does not activate LGR5 ISC proliferation under homeostasis but restores the population to counteract intestinal epithelial damage post-injury. However, the potential impact of IPA on carcinogenesis requires further investigation.

Our data suggests that IPA accelerates LGR5<sup>+</sup> ISC restoration and promotes epithelium regeneration during mucosal injury in a PPAR $\alpha$ - and HMGCS2-dependent manner. The impact of IPA on modulating PPAR $\alpha$  transcriptional activity has not been reported. Furthermore, the present study has uncovered, for the first time, that Tyr314 and Ile317 in the PPAR $\alpha$  LBD are key binding sites for IPA, playing an essential role in the IPA-induced upregulation of PPAR $\alpha$  transcriptional function (Fig. 7k–n).

While our findings demonstrate the therapeutic potential of supraphysiological IPA administration in driving mucosal repair, we acknowledge the current limitations in fully delineating the physiological contribution of microbiota-derived IPA at endogenous concentrations. The inherent complexity of gut microbial ecosystems—marked by interindividual variability in bacterial composition, host-microbe metabolic crosstalk, and dynamic shifts during inflammation—poses challenges in precisely correlating baseline microbial IPA production with ISC-mediated barrier restoration. Our experimental models, while pharmacologically informative, cannot fully recapitulate the spatiotemporal dynamics of microbial metabolite gradients in the crypt niche. Thus, establishing definitive causality between physiological IPA levels and PPAR $\alpha$ -mediated ketogenesis in both human and mice IBD models requires further investigation.

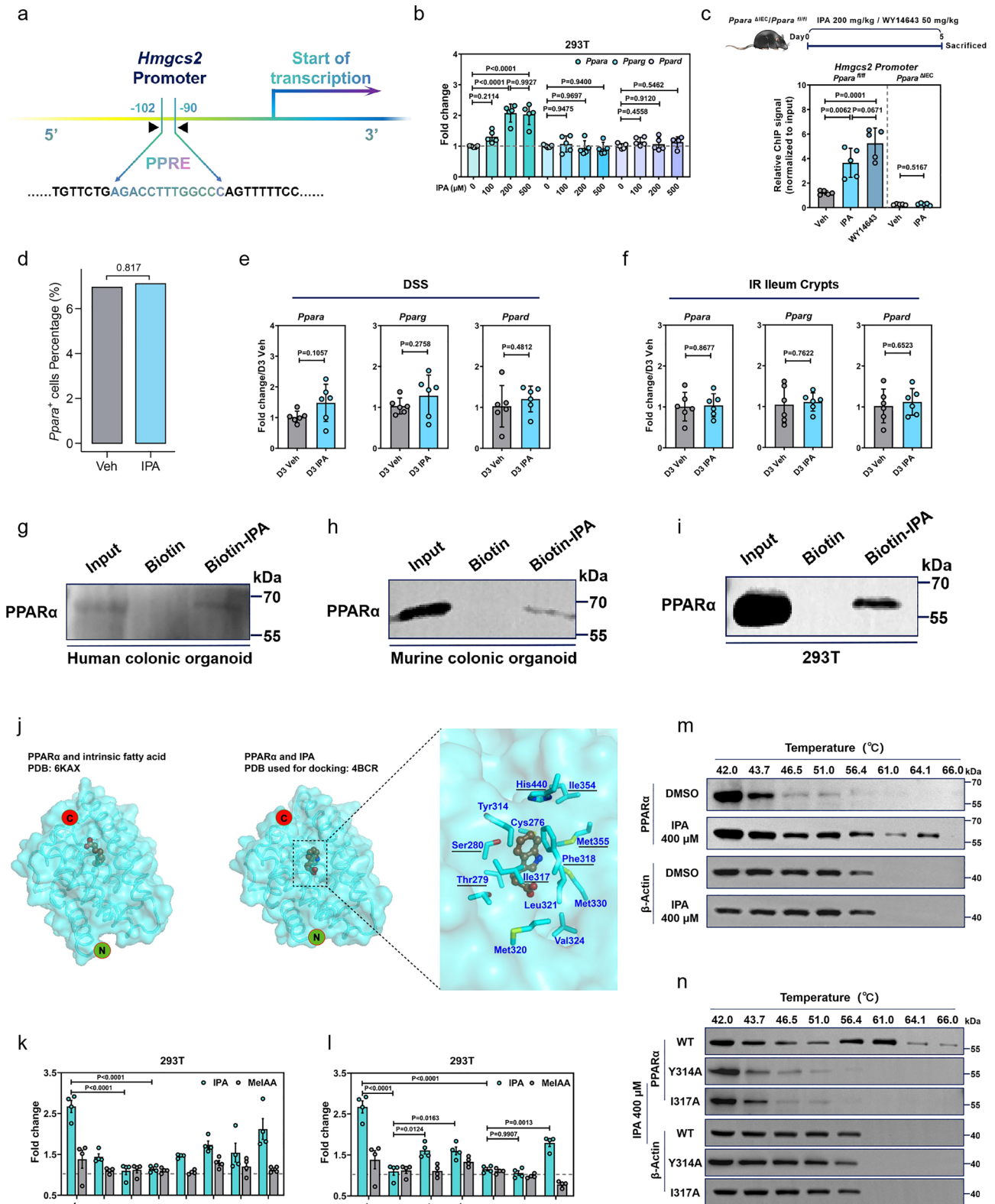
IBD is characterized by adverse alterations in the composition and metabolic profiles of the gut microbiota (termed as dysbiosis). Analysis of publicly available microbiome metagenomes has pointed to a

significant underrepresentation of *P. russellii* in IBD cohorts from distinct geographic areas (Fig. 8a–d), yet establishing a clear clinical connectivity between *P. russellii* and IBD is challenging due to the limited access to fecal samples from IBD patients throughout the course of the disease. Nevertheless, in our well-controlled DSS-induced colitis mouse model, we were able to demonstrate a definitive protective role of *P. russellii* in monocolonization assays in GF mice, reflected by mitigated colitis and improved mucosal barrier function (Fig. 8m–q). The beneficial effects of *P. russellii* on mucosal barrier function have also been underscored by Wlodarska et al., who demonstrated that *P. russellii* colonization in conventional mice led to improved goblet cell differentiation and reduced inflammatory signals, driven by the production of Trp metabolites IPA and IA<sup>29</sup>.

Although mono-colonization with *P. russellii* elevates IPA and confers colitis protection in gnotobiotic models, direct comparison with FMT-colonized mice introduces substantial interpretative complexity. FMT-reconstituted microbiota harbor multifaceted variables beyond IPA, including immunomodulatory commensals such as segmented filamentous bacteria (SFB) that may independently drive inflammation<sup>32</sup>. The significantly reduced IPA levels in FMT-colonized GF mice relative to conventional donors further suggest inadequate functional engraftment of IPA-producing consortia.

Current IBD treatments predominantly exert their therapeutic effects by suppressing immune responses, often achieved by inhibiting specific inflammatory mediators such as TNF $\alpha$ <sup>33,34</sup>. The resultant immunosuppression can lead to infectious and neoplastic complications, which may significantly impact the lives of IBD patients and pose great clinical challenges for healthcare providers<sup>34,35</sup>. The absence of effective therapeutic strategies, coupled with the intricate nature of disease mechanisms that influence diverse inflammatory pathways, renders the idea of inducing mucosal healing without the need for direct immunosuppression a compelling therapeutic goal. Using the DSS-induced colitis model, our findings suggest that IPA supplementation and *P. russellii* colonization drive therapeutic efficacy against IBD, significantly enhancing mucosal repair while conferring epithelial barrier protection.

Our research has certain constraints that must be taken into account. (1) Elucidating the cellular origins of BHB production during post-injury recovery presents persistent technical challenges, as current methodologies struggle to achieve high-purity isolation of specific cell populations in colitis models required for direct quantification of cell-autonomous BHB synthesis. (2) Although patients with CD were selected based on their initial diagnosis and were treatment-naïve prior to fecal sample collection, the 1-month exclusion window for antibiotics usage is relatively short. Therefore, we could not entirely exclude the influence of past antibiotic use on the microbiota of CD patients, which might affect our human study results. (3) The exact mechanism by which IPA promotes PPAR $\alpha$  transcriptional activity need to be further investigated with a purified LBD domain. (4) Future studies on *P. russellii* mutants deficient in Trp transformation may provide key evidence for the direct involvement of IPA in the *P. russellii*-dependent mechanisms that drive the reconstruction of LGR5<sup>+</sup> ISCs and epithelial regeneration in response to mucosal injury. (5) Future studies should also employ defined microbial communities (with and without *P. russellii*) to more rigorously assess the specific



contribution of *P. russellii*-derived IPA to mucosal protection within a controlled polymicrobial context. (6) Further validation and clinical intervention studies are necessary to determine whether *P. russellii* or IPA can be established as reliable biomarkers for assessing risk, predicting outcomes, or guiding therapeutic strategies in IBD management.

In conclusion, our study establishes that microbiota-derived IPA can facilitate the HMGCS2-mediated production of BHB in IECs to restore LGR5<sup>+</sup> ISC population in a PPARα-dependent manner. The findings from our research may offer potential avenues for targeted interventions that could help modulate the complex interactions between the host and its endogenous microbial community.

**Fig. 7 | IPA activates PPAR $\alpha$ -dependent transcription by binding to its ligand-binding domain.** **a** Schematic of *Hmgcs2* promoter PPRE motif. **b** Dose-dependent PPAR $\alpha$ / $\gamma$ / $\delta$  activation by IPA (100–500  $\mu$ M) in 293 T cells co-transfected with PPRE-luciferase and control vector plasmids ( $n = 5$ ). **c** In vivo schematic: *Ppara*<sup>fl/fl</sup> and *Ppara*<sup>fl/EC</sup> mice with or without IPA/WY14643 treatment followed by crypt ChIP-qPCR ( $n = 5$ ). **d** *Ppara*<sup>fl</sup> cell frequency in DSS-exposed crypts (scRNA-seq). **e, f** PPAR isotype expression in IPA-treated crypts from DSS (**e**) and radiation enteritis (**f**) models ( $n = 6$ ). **g–i** Biotin-IPA pull-down assays in human organoids (**g**), murine

crypts (**h**), and 293 T lysates (**i**). **j** Molecular docking of IPA-PPAR $\alpha$  complex: crystal structure (left), binding pose (middle), residue interactions (right; PPAR $\alpha$  cyan, ligand brown). **k, l** PPRE-luciferase activity in 293 T cells transfected with wild-type or mutant *Ppara* with or without IPA/MelAA ( $n = 4$ ). **m, n** CETSA validating IPA-PPAR $\alpha$  binding in *Ppara*-wild or *Ppara*-mutant transfected 293 T cells. Data represent mean  $\pm$  SD from  $\geq 2$  independent experiments. Statistical significance determined by two-sided Student's t-test or one-way ANOVA followed by Tukey's post hoc test for multiple comparisons. Source data are provided as a Source data file.

## Methods

### Cell lines and treatment

293 T cells were grown in Dulbecco's modified Eagle medium (DMEM, Meilunbio, MA0212), supplemented with 10% fetal bovine serum (FBS) (Gibco, A5669701) and 1% penicillin/streptomycin solution (Meilunbio, MA0110). They were kept at 37 °C in a humidified atmosphere containing 5% CO<sub>2</sub>.

### Microbe strains

All microbe strains were described in the Supplementary Table 1. *Peptostreptococcus russellii* (*P. russellii*) was cultured in chopped meat carbohydrate broth (CMC) medium (TOPBIO) at 37 °C for 48 h under an atmosphere of 10% CO<sub>2</sub>, 10% H<sub>2</sub> and 80% N<sub>2</sub> in an anaerobic incubator (AW300SG, Pummiero Scientific). *Clostridium sporogenes* (*C. sporogenes*) was grown in MRS medium (LAND BRIDGE, CM187) at 37 °C under the same anaerobic conditions (10% CO<sub>2</sub>, 10% H<sub>2</sub>, 80% N<sub>2</sub>) for 48 h.

For metabolite supplementation studies, culture media were supplemented with varying concentrations of L-tryptophan (Trp) as specified in respective figures, followed by sterilization via autoclaving. All bacterial strains were cultured in biological triplicate under anaerobic conditions (37 °C, 10% CO<sub>2</sub>, 10% H<sub>2</sub>, 80% N<sub>2</sub>). Uninoculated media served as negative controls. Following 48-h fermentation, optical density at 600 nm (OD<sub>600</sub>) was quantified using a spectrophotometer (BioTek Synergy H1), after which cultures were immediately chilled on ice. Cellular fractions were separated by centrifugation (16,000  $\times$  g, 10 min, 4 °C; Eppendorf 5424R), with 1 mL aliquots processed per sample. Resultant supernatants were aliquoted and stored at –20 °C pending metabolomic analysis.

### Bacterial count

After 48 h of culture, the bacteria were collected and serially diluted 10-fold on respective culture plates and CFUs were counted after 16 h incubation at 37 °C. Specifically, *P. russellii* dilutions were cultured on Trypticase soy agar with defibrinated sheep blood under anaerobic conditions in an anaerobic incubator (AW300SG, Pummiero Scientific). The bacterial cells were then pelleted by centrifugation at 6000  $\times$  g at 4 °C for 10 min, washed, and resuspended in sterile reduced PBS buffer to achieve a specific density suitable for mouse gavage. These operations were conducted under anaerobic conditions in an anaerobic incubator (AW300SG, Pummiero Scientific).

### Human participants

Fecal samples were collected from 34 healthy controls (aged 18 to 73, with no psychological or cognitive impairments) and from 39 patients with Crohn's disease (CD) at Sir Run Run Shaw Hospital, School of Medicine, Zhejiang University (Supplementary Table 1). All patients were diagnosed according to European Crohn's and Colitis Organization (ECCO) guidelines, including radiologic, endoscopic, clinical symptoms, and pathology. The patients were without antibiotics and probiotics in the month prior to sample collection. Other exclusion criteria included: history of bowel resection; pregnant or lactating women; age <18, or age >75. The baseline characteristics of the participants are shown in Supplementary Data 1. Stool samples were collected right after defecation and snap frozen for LC-MS/MS

analysis. Informed consent was obtained from all participants, and the experimental protocol was approved by the Clinical Research Ethics Committee of the Clinical Research Ethics Committee of Sir Run Run Shaw Hospital, Zhejiang University School of Medicine (20210622-31).

Human colonic biopsies were collected at the First Affiliated Hospital of Guangdong Pharmaceutical University. Three individuals underwent colonoscopy as part of their routine health examinations, necessitating tissue removal for pathological biopsy due to the presence of intestinal polyps. Fresh normal mucosal tissues, either utilized for human organoid culture or immersed in a 4% paraformaldehyde solution for immunofluorescence assay (IFA), were obtained from healthy regions of the intestinal tissue adjacent to the polyps, as identified and assessed by the physician during the tissue acquisition process. Informed consent was obtained from all participants, and the experimental protocol was approved by the Clinical Research Ethics Committee of the First Affiliated Hospital of Guangdong Pharmaceutical University (V1.0, 20210221). Participants did not receive financial compensation.

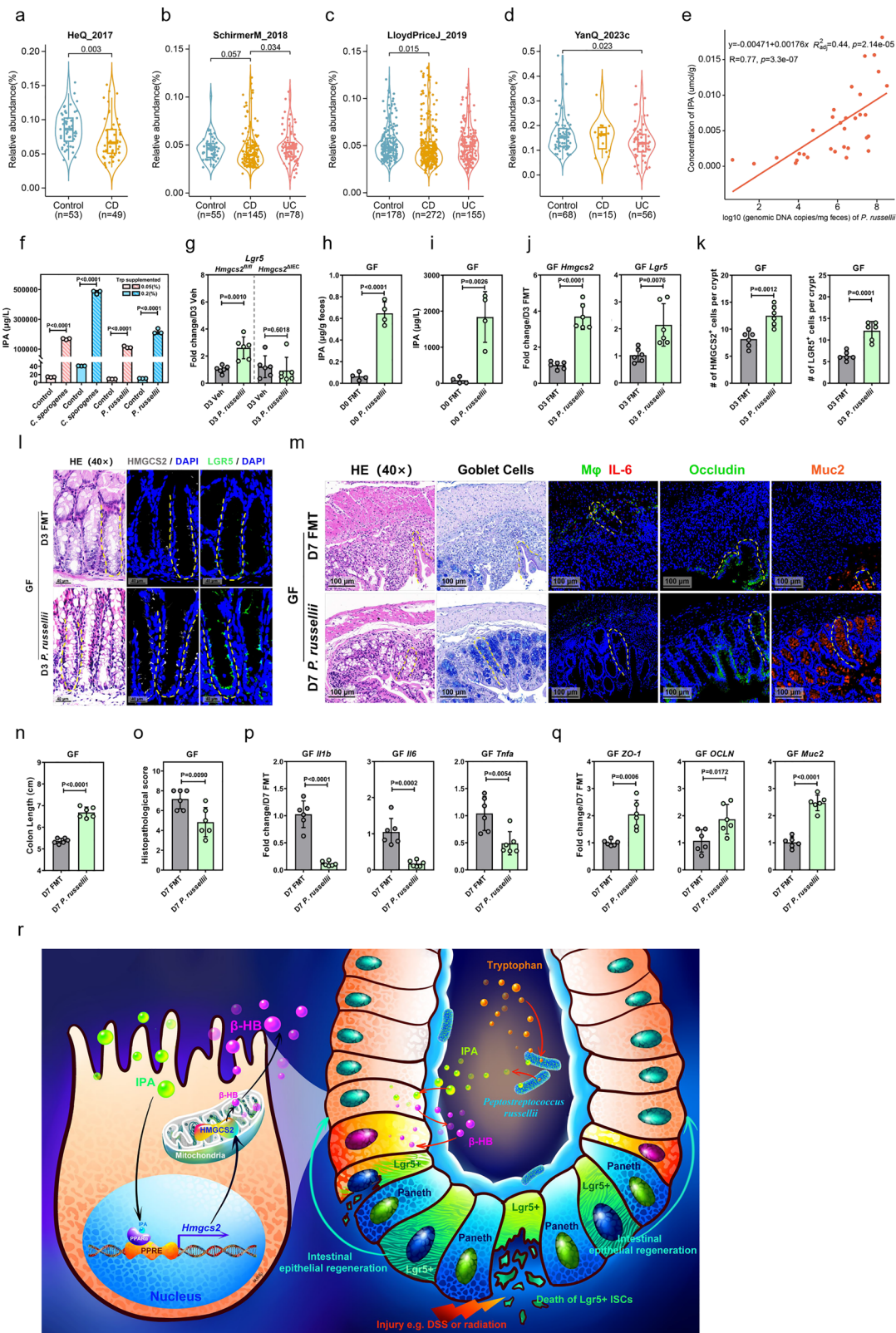
### Animals

All experiments used mice were described in the Supplementary Table 1. Germ-free (GF) C57BL/6J mice were bred and housed at the Shenzhen Gnotobio Biotechnology Co., Ltd. GF status was confirmed through 16S qPCR analysis before use in relevant experiments, which were also carried out at Shenzhen Gnotobio Biotechnology Co., Ltd. Wild-type C57BL/6J (WT) mice were purchased from the Model Animal Research Center of Nanjing University (Nanjing, China). *Nlrp3*<sup>–/–</sup> mice, *Ahr*-flox mice and *Villin*-Cre mice were purchased from Cyagen Biosciences Inc. (Suzhou, China). *Ppara*-flox mice were kindly provided by Dr. Aijuan Qu from Department of Physiology and Pathophysiology, School of Basic Medical Sciences, Capital Medical University. *Hmgcs2*-flox mice were a gift from Dr. Kai Xia from National-Local Joint Engineering Research Center for Stem Cells and Regenerative Medicine, Zhongshan School of Medicine, Sun Yat-sen University. *Pxr*<sup>–/–</sup> mice generously provided by Dr. Jie Yin from Hunan Agricultural University. The *Lgr5*-CreERT2 mice and *H11-CAG-LSL-tdTomato* mice were purchased from GemPharmatech Co., Ltd (Nanjing, China).

Unless otherwise stated, all experiments utilized 6–8-week-old male or female mice. No significant sex-dependent differences were observed in the reported experiments. The mice were housed in a specific-pathogen-free (SPF) facility at Zhejiang University, where they were maintained under controlled conditions of temperature (22  $\pm$  2 °C) and humidity (50  $\pm$  10%), with a constant 12-h light/dark cycle. They had free access to a regular chow diet (P1101F-25, Suzhou SHUANGSHI) and water throughout the study (detailed composition in Supplementary Data 2). They had free access to a regular chow diet (P1101F-25, Suzhou SHUANGSHI) and water throughout the study. The ethical guidelines of the Animal Experimentation Ethics Committee of Zhejiang University (No. 27248) and IACUC of Gnotobio (JTAW20240615-1) were followed.

### Colitis models and treatments

Unless otherwise specified, WT or certain knockout mice were administered 2.5% dextran sulfate sodium (DSS, Yeasen, 60316ES76) in their



drinking water for 7 days to establish the DSS-induced colitis mouse model.

To assess the impact of bacterial strains on DSS-induced colitis, *Hmgcs2<sup>fl/fl</sup>* and *Hmgcs2<sup>ΔIEC</sup>* mice were gavaged with 200 μL of PBS containing 10<sup>9</sup> CFU of *P. russellii* twice within a 48-h interval, followed by DSS treatment. GF mice were similarly treated with 200 μL of PBS containing 10<sup>6</sup> CFU of *P. russellii* twice within a 48-h interval, followed

by DSS treatment. The control group received an equal volume of PBS via gavage.

Mice were administered IPA via different routes and dosages as previously described. Specifically, mice were gavaged with IPA at 200 mg/kg (insoluble, suspend thoroughly before gavage, 200 μL PBS per mouse) daily<sup>36</sup>, or at a lower dose of 20 mg/kg (solution, 0.5 mg per 200 μL PBS) daily for 5 days<sup>37,38</sup>, or treated with IPA at a concentration

**Fig. 8 | *P. russellii* produces IPA and improves HMGS2-mediated LGR5<sup>+</sup> ISC proliferation.** **a–d** Violin plots overlaid with boxplots depict metagenomic abundances of *P. russellii* in patients with IBD and healthy controls across four independent cohorts. The width of each violin represents the kernel density estimation of the data distribution. Boxes represent the interquartile range between the first and third quartiles and the median (internal line). Whiskers denote the lowest and highest values within 1.5 times the range of the first and third quartiles, respectively; dots represent outlier samples beyond the whiskers. Individual points represent single samples. **e** Two-sided Spearman's rank correlation and two-sided linear regression analysis between IPA and *P. russellii* in CD cohort ( $n = 32$ ). **f** IPA

production by *P. russellii* vs *C. sporogenes* in Trp-supplemented media ( $n = 3$ ). **g** *Lgr5* expression in crypts isolated from *Hmgcs2<sup>fl/fl</sup>* and *Hmgcs2<sup>ΔIEC</sup>* mice colonized with  $10^9$  CFU *P. russellii* post-DSS ( $n = 6$ ). **h, i** Fecal/serum IPA in GF mice colonized with FMT or *P. russellii* ( $n = 4$ ). **j–q** GF-DSS model colonized with FMT/*P. russellii* ( $n = 6$ ): D3 ketogenesis/ISC markers (**j–l**); D7 phenotypes (**m–o**); qRT-PCR of *Il1b*, *Il6*, *Trnfa* in colon and *OCLN*, *ZO-1*, *Muc2* in cIECs (**p, q**). **r** Mechanistic schema of *P. russellii*-IPA-HMGS2 axis. Data represent mean  $\pm$  SD ( $\geq 2$  experiments). Two-sided Wilcoxon rank-sum tests (**a–d**) with BH adjusted *P* values, and two-sided *t*-tests (**f–q**) were used to assess statistical significance. Source data are provided as a Source data file.

of 200  $\mu\text{g}/\text{mL}$  in their drinking water for 14 days before DSS treatment<sup>39</sup>. In the IPA water treatment, daily consumption of 6–8-week-old mice (20–25 g bodyweight) has been documented as 3.7 to 4.5 mL per mouse, thus the daily IPA intake of this route is ranged from 0.74 mg to 0.9 mg.

To evaluate the therapeutic potential of IPA in experimental colitis without pretreatment, conventional WT mice were first treated with 2.5% DSS in drinking water for 5 days. Subsequently, they were gavaged with IPA at 200 mg/kg for 5 days, followed by regular water administration.

For the  $\beta$ -hydroxybutyrate (BHB) protection study, mice were gavaged with BHB at 40 mg/25 g (dissolved in 100  $\mu\text{L}$  PBS) 16 h before DSS treatment. In the PPAR $\alpha$  agonist experiments, mice were intraperitoneally injected with WY14643 at 50 mg/kg (dissolved in 100  $\mu\text{L}$  of 10% DMSO and 90% corn oil) daily for 5 days.

For the 2,4,6-trinitrobenzene sulfonic acid (TNBS) model, mice were shaved on the back just below the neck and painted with 1% TNBS (Meilunbio, MB5523) mixed in an acetone/olive oil solution for pre-sensitization (150  $\mu\text{L}$  per mouse). After 7 days of pre-sensitization, mice were anesthetized and maintained with 1.5% to 2.0% isoflurane. Subsequently, 2.5% TNBS in 100  $\mu\text{L}$  of 50% ethanol solution was administered into the colon via a catheter inserted approximately 3 cm into the anus.

### Radiation enteritis (RE) model

WT mice were anesthetized by intraperitoneal injection of 50 mg/kg Zoletil<sup>®</sup> 50 (virbac) and 5 mg/kg Xylazine Hydrochloride (D005, Jilin Huamu Animal Health Product Co., Ltd.), then treated with total abdominal irradiation with a single irradiation dose of 16 Gy (y-ray) at a rate of 1.0 Gy/min in a Siemens Primus Plus (SIEMENS, Germany) to establish a radiation enteritis (RE) model.

### Fecal microbiota transplantation (FMT)

For FMT experiments, 200 mg of fresh pooled fecal pellets from WT mice were homogenized with sterile grinding beads in 1.5 mL PBS at 45 Hz for 1 min and filtered with 70  $\mu\text{m}$  strainers. GF mice were subjected to gavage with 150  $\mu\text{L}$  filtered stool homogenates containing  $10^7$  CFU of commensal bacteria twice within a 48-h interval. At 48 h after FMT or bacterial colonization, stool samples were collected to determine the efficiency of colonization prior to DSS administration for colitis model induction.

### Fecal bacteria quantification

Fecal bacterial DNA was extracted using the TIANamp Stool DNA Kit (TIANGEN), and quantitative PCR (qPCR) was conducted with SYBR Green Real-time PCR Master Mix (TOYOBO). The quantification of *P. russellii* was achieved through the use of standard curves, which were constructed from cloned DNA amplified with conserved specific primers (primers are detailed in the Supplementary Table 1).

### Isolation of intestinal epithelial cells (IECs) and lamina propria mononuclear cells (LPMCs)

Murine IECs and LPMCs were obtained from the colon and ileum as previously described<sup>40</sup>. Briefly, the colon and ileum were longitudinally

opened and cut into pieces. These pieces were then incubated with EDTA (5.5 mM) and dithiothreitol (DTT) (1 mM) in Hank's balanced salt solution (HBSS). Following vortexing and passage through a 70  $\mu\text{m}$  strainer, the suspension of IECs was washed twice by centrifugation at  $600 \times g$  for 3 min and collected for subsequent experiments. The remaining lamina propria tissue was further processed by incubating with a digestion solution containing collagenase (1 mg/mL) and DNase (0.2 mg/mL). The resulting LPMC suspension was subjected to Percoll-gradient separation and harvested for further analysis.

### Quasi-targeted metabolomics

Metabolites were extracted from fecal samples of human origin and subsequently sent to BGI (Shenzhen, China) for targeted metabolomics analyses. High-performance LC-MS/MS was used to perform high-sensitivity, wide-coverage, and high-throughput HM700-targeted quantification of 700 metabolites in these samples (<https://www.bgi.com/global/service/hm700>). In detail, appropriate amounts of experimental or quality control (QC) samples were resuspended in 140  $\mu\text{L}$  of a 50% water/methanol solution, lysed, and centrifuged, and the supernatant was transferred to a new tube. A standard curve was prepared by serial dilution of an HM700 mixed standard. The experimental sample, QC sample, and standard were subjected to a derivatization reaction, and the resulting compounds were diluted in HM700 diluent and centrifuged at  $12,000 \times g$  at 4 °C for 10 min. The supernatant was applied to LC-MS/MS analysis on an LC-MS QTRAP 6500 Plus (SCIEX, USA). Chromatographic separation was performed on a BEH C18 column (2.1  $\times$  100 mm, 1.7  $\mu\text{m}$ ; Waters). The mobile phases consisted of water containing 0.1% formic acid (solvent A) and acetonitrile containing 30% isopropanol (solvent B). Chromatographic separation was performed on a BEH C18 column (2.1 mm  $\times$  100 mm, 1.7  $\mu\text{m}$ ; Waters). Elution was carried out using the following linear gradient: 0–1.00 min, 5% B; 1.00–5.00 min, 5–30% B; 5.00–9.00 min, 30–50% B; 9.00–11.00 min, 50–78% B; 11.00–13.50 min, 78–95% B; and 13.50–14.00 min, 95–100% B, at a flow rate of 0.400 mL/min. The column was then washed at 100% B from 14.00 to 16.00 min at a flow rate of 0.600 mL/min, followed by re-equilibration at 5% B from 16.00 to 18.00 min at a flow rate of 0.400 mL/min. The column temperature was maintained at 40 °C. Mass spectrometric analysis was performed using an electrospray ionization source operated in both positive and negative ion modes (ESI+ and ESI–). The ion source parameters were set as follows: ion source temperature, 400 °C; ion spray voltage, 4500 V in positive mode and –4500 V in negative mode; ion source gas 1 (GS1), ion source gas 2 (GS2), and curtain gas (CUR) were set to 60, 60, and 35 psi, respectively. Data acquisition was conducted in multiple reaction monitoring (MRM) mode using a targeted MRM method that included precursor–product ion transitions, collision energy (CE), declustering potential (DP), and retention time information for each target metabolite. Skyline software (v24.1)<sup>41</sup> was utilized to identify and qualify the metabolites for each sample, using the following parameters: “Mass: Monoisotopic peaks, Mass Tolerance: 0.6 Da, Mass Range: 50–1500 Da.” Subsequently, probabilistic quotient normalization and quality control-robust spline signal correction based on QC samples were applied to the metabolomic profile using the *metaX* R package (v1.4.2). Classification and functional annotation of

metabolites were performed based on the Human Metabolome Database (HMDB, <https://hmdb.ca/>) and the Kyoto Encyclopedia of Genes and Genomes (KEGG) database (<https://www.genome.jp/kegg/>). Partial least squares discrimination analysis (PLS-DA) was employed to identify differentially abundant metabolites between groups, utilizing the 'opls' function with parameters "orthol=0" from the *ropls* R package (v1.34). Meanwhile, the Wilcoxon rank-sum test, followed by Benjamini–Hochberg (BH) adjustment was used to access significant differences in the metabolite concentration between two groups. A metabolite was considered significantly enriched if its VIP value exceeded 1 or its adjusted *P*-value was below 0.05. Furthermore, KEGG pathway enrichment analyses were performed on differential abundance metabolites using the 'enricher' function from the *ClusterProfiler* R package (v4.14.6)<sup>42</sup>, utilizing the pathway-metabolite relationships (<http://rest.kegg.jp/link/pathway/compound>). The metabolite profile of human feces is provided in Supplementary Data 3.

### β-Hydroxybutyrate (BHB) analysis

Serum, cIECs and liver tissues from murine models, organoid culture supernatants from human and murine organoid were collected for BHB measurement. Liver tissues (50 mg) and cIEC pellets harvested from colon tissues (-7 cm) were homogenized with sterile grinding beads in 500 μL PBS at 45 Hz for 1 min, centrifuged (6000 × *g*, 5 min, 4 °C) to collect the supernatant and divided in two aliquots for total protein and BHB measurement. Levels of BHB were normalized to the total protein content. Total protein was measured by BCA Protein Assay Kit (EpiZyme, ZJ101) and BHB level was determined by BHB Assay Kit (Solarbio, BC5085) following the manufacturer's instructions.

### Determination of Indole-3-propionic acid (IPA) and tryptophan (Trp) by LC-QQQ/MS

For fecal and colon samples, 100 mg of the sample was weighed into a 2 mL centrifuge tube, and 1 mL of 50% methanol was added to homogenize. Metabolites were extracted using ultrasonic treatment in an ice bath for 30 min and then centrifuged for 10 min at 12,000 rpm. The supernatant was used for analysis by LC-QQQ/MS. For serum and culture supernatant samples, 0.8 mL of a methanol/acetonitrile mixture (1:1, V/V) was added to 0.2 mL of the sample. The mixture was thoroughly vortexed, and proteins were precipitated at -20 °C for 2 h. The mixture was then centrifuged for 10 min at 12,000 rpm, and the supernatant was used for analysis by LC-QQQ/MS.

Analyses were carried out on a Shimadzu high-performance LC system, Nexera X2 LC-30AD (Kyoto, Japan). Separations were performed on an Acquity BEH C18 column (2.1 × 100 mm) with 1.7 μm particles from Waters (Milford, MA, USA), maintained at 40 °C during separation. The mobile phase consisted of water containing 0.1% formic acid (Phase A) and acetonitrile containing 0.1% formic acid (Phase B). The flow rate was set at 0.3 mL/min, and the injection volume was 1 μL, employing a gradient elution profile as follows: 0–1 min, 3% B; 1–3 min, 3% B to 20% B; 3–3.5 min, 20% B to 80% B; 3.5–6 min, 80% B; 6–6.5 min, 80% B to 3% B; 6.5–9 min, 3% B. Detection was performed using a 5500 Series ion trap from AB SCIEX equipped with an ESI source. The source parameters were set as follows: temperature 550 °C, Ion Source Gas 1 (GS1) 55, Ion Source Gas 2 (GS2) 55, Curtain Gas (CUR) 35, Ion Spray Voltage (IS) 5500 V. Metabolites were detected in positive multiple reaction monitoring (MRM) mode, with the ion pairs 190 > 130 and 190 > 172 for IPA, and 205 > 188 and 205 > 146 for Trp.

Quantitative analysis was performed via external calibration with linearity established through peak area-concentration plots of standard solutions. Method sensitivity was determined by signal-to-noise ratios of 3 and 10 for limits of detection (LOD, 0.25 ng/mL) and quantification (LOQ, 0.83 ng/mL), respectively. Intra-day precision (2.05% RSD) was evaluated through six replicate analyses of standard solutions, while repeatability (2.26% RSD) was assessed using six

independently prepared samples. Recovery rates (96.56%) were calculated using the standard addition method: (observed amount – original amount)/spiked amount × 100%. The UPLC-QQQ/MS method demonstrated excellent linearity for IPA (*r* = 0.9999) across a broad concentration range, as detailed in Supplementary Data 4. Validation confirmed the method's robustness, featuring low detection limits, high precision, and reliable accuracy for IPA quantification.

### Flow cytometry analysis

1 × 10<sup>6</sup> cLPMCs were incubated with 1 mg of anti-CD16/32 antibody (BioLegend, 101320) for 10 min to block non-specific binding of immunoglobulin to the Fc receptors. Subsequently, cells were stained for live cells using the Live/Dead Fixable Aqua Dead Cell Stain Kit (BD Biosciences, 564995) for 30 minutes. Following this, the appropriate amount of pre-diluted fluorescent-labeled antibodies (eBioscience, 11-0032-82, 48-0041-82, 11-9668-80; MultiSciences, F41011b04, F21480A02; Tonbo Biosciences, 20-0081; Biolegend, 117309) was added to each tube as per the manufacturer's recommendations. The cells were then incubated in the dark at 4 °C for 30 min and washed twice with PBS. Flow cytometry was conducted using the FACSVerser system (BD Biosciences) with FSC and SSC thresholds set at 1000 and a logarithmic scale. Between 30,000 and 150,000 events were recorded and analyzed using FlowJo software (Tree Star). The gating strategy is detailed in Supplementary Fig. 1h.

### Pull-down assays

For biotin-IPA pull down assays, magic Dynabeads MyOne Streptavidin T1 was pre-incubated with either free biotin or biotin-IPA in PBS for 1 h at room temperature, then washed with 0.01% PBST (PBS, pH 7.4, 0.01% Tween-20), and incubated with cell lysates for 3 h at 4 °C. The beads were washed four times with 0.01% PBST and analyzed by immunoblot.

### PPARα site-directed mutagenesis

A pEF-BOS plasmid containing murine *Ppara* gene, as described in a previous literature<sup>43</sup>, was utilized to generate PPARα mutant constructs. Site-directed mutagenesis of PPARα was performed using a PCR mutagenesis strategy, with the primers used in this study detailed in the Supplementary Table 1. High-fidelity enzyme was used for PCR amplification. The mutagenesis PCRs were performed with the following conditions: PCR mix: 19 μL H<sub>2</sub>O, 2 μL 10 μM forward primer, 2 μL 10 μM reverse primer, 2 μL 20 ng/μL template plasmid (*Ppara*-wild), and 25 μL 2 × Phanta Max Master Mix (Vazyme, P515). Cycling conditions: (1) 95 °C/30 s (2) 95 °C/10 s (3) 61 °C/30 s (4) 72 °C/5 min (5) Return to Step 2 for 34 cycles (6) 72 °C/5 min. After the PCR reaction, 1 μL of DpnI (NEB, R0176) was added to the PCR reaction mixture and incubate at 37 °C overnight. Then the digested product was transformed into chemically competent *E. coli* DH5α (Yeasen, 11802ES80) following the manufacturer's instructions. Select colonies on LB plates, perform shaking and sequencing to confirm the mutation. Plasmid extraction was used the FastPure EndoFree Plasmid Maxi Kit (Vazyme, DC202).

### Molecular docking analysis

The structure of PPARα (PDB ID: 4BCR) was retrieved from the RCSB PDB Protein Data Bank (<http://www.rcsb.org>). Additionally, the structure of indole-3-propionic acid (IPA, chemical component identifier: IOP) was obtained from the Ligand Expo of the Protein Data Bank (<http://ligand-expo.rcsb.org/ld-search.html>). The docking of these two molecules was conducted using HDock as previously described<sup>44</sup>, and the results were visualized using PyMOL (v3.2).

### Dual luciferase reporter assay

For the luciferase assay, 293 T cells were cultured in 24-well plates at 70 to 80% confluency and co-transfected with the plasmids encoding

*Ppara*-wild, *Ppara*-mut, *Pparg*-wild, or *Ppard*-wild, along with the PPRE plasmid and a control vector (Renilla luciferase), using Lipofectamine 3000 Reagent (Invitrogen, L3000150) according to the manufacturer's protocols. Mouse *Pparg* (variant 2) ORF clone (MR208132) and Mouse *Ppard* ORF clone (MR207001) were purchased from OriGene Technologies, Inc. (Wuxi, Jiangsu, China). The expression plasmid for the PPRE reporter, as previously described<sup>45</sup>, was utilized in the assay. After 24 h of transfection, the cells were incubated with IPA and indole-3-methyl acetate (MeIAA) at the indicated doses for an additional 6 h before analysis. Subsequently, the cells were harvested and lysed, and the activities of firefly and Renilla luciferases were measured using the Dual Luciferase Reporter Gene Assay Kit (Beyotime, RG028) as per the manufacturer's instructions. Each sample was tested in triplicate, and the transfections were repeated, with the number of replicates detailed in the figure legends.

### Cellular thermal shift assay (CETSA)

The binding efficiency of IPA to the PPAR $\alpha$  protein in 293 T cells was determined using CETSA. Briefly, 293 T cells were cultured overnight in a 100  $\times$  20 mm Petri dishes, then the cells were transfected with the *Ppara*-wild or *Ppara*-mut plasmid. After 24 h of transfection, cells were further incubated with or without IPA (400  $\mu$ M) for another 6 h before analysis. Then the cells were collected and divided equally into eight aliquots; each aliquot was heated at a specified temperature (42–66  $^{\circ}$ C) for 10 min and cooled to ambient for 3 min. The samples were then quickly frozen and thawed in liquid nitrogen for 3 cycles, centrifuged at 12,000 rpm for 5 min at 4  $^{\circ}$ C and the supernatant was collected. Western blotting was used to detect the expression of PPAR $\alpha$  at various temperature gradients.

### Isolation of crypts, culture of intestinal organoids and treatments

For murine organoid culture: ileum and colon tissues of mice were removed, wash with cold PBS, opened longitudinally, cut into pieces and then incubated on ice in buffer (1 $\times$ PBS, 8 mM EDTA, 0.5 mM DTT) for 20–45 min. Crypts were then mechanically separated from the connective tissue by shaking, and filtered through a 70  $\mu$ m mesh into a 50 mL conical tube to remove villus material and tissue fragments. Isolated crypts were centrifuged for 2 min at 68  $\times$  *g*, resuspended in organoid growth medium for organoid culture.

Murine colonic organoids were cultured as previously described<sup>16</sup>. Briefly, isolated crypts were centrifuged for 2 min at 68  $\times$  *g*, resuspended in the appropriate volume of cold mouse colonic organoid growth medium (bioGenous, K2204-MC) and embedded in equal volume of Matrigel matrix (ABW, 082703) at 50–250 crypts/20–30  $\mu$ L in a 48-well plate. The crypts/Matrigel mixture was allowed to solidify for 15–20 min in a 37  $^{\circ}$ C incubator and then overlaid with additional 200  $\mu$ L organoid growth medium. After 4-day culture, organoids were dissociated in organoid dissociation solution (bioGenous, E238001) for 2 min at 37  $^{\circ}$ C according to the manufacturer's protocol, centrifuged at 68  $\times$  *g* for 2 min, resuspended in organoid culture medium, and cultured as described above for organoids passaging. After culture for 2 day, 100  $\mu$ M IPA was added to organoids and incubated at 37  $^{\circ}$ C for 6 h. For the BHB pretreatment, 10 mM BHB was added to organoids and incubated at 37  $^{\circ}$ C for 3 h. To establish pathological conditions for inflammation, IFN- $\gamma$ /TNF- $\alpha$  (20 ng/mL each) was added for 18 h.

For human organoid culture: adult human organoids were prepared from endoscopy samples obtained from non-IBD individuals. Crypts isolation and organoid culture methods are consistent with mice. Human colonic organoid kit (K2003-HC, bioGenous) was used for human organoid growth medium. At day 3, 200  $\mu$ M IPA and 10 mM BHB was added to organoids and incubated at 37  $^{\circ}$ C for 6 h or 3 h. To establishing pathological conditions for inflammation, IFN- $\gamma$ /TNF- $\alpha$  (187.5 ng/mL each) were added for 24 h or 48 h.

### Chromatin immunoprecipitation (ChIP)-qPCR assay and analysis

ChIP assay was performed according to the manufacturer's protocol (Thermo Scientific, 26157). Briefly, colon crypts were isolated and cross-linked with 1% formaldehyde at room temperature for 10 min, after which the cross-linking was quenched using Glycine Solution. Following centrifugation, the resulting pellet was lysed in the specified lysis buffer supplemented with a protease inhibitor cocktail. The extracted genomic DNA was then enzymatically digested to achieve DNA fragmentation using micrococcal nuclease. A 5  $\mu$ L aliquot of the supernatant containing the digested chromatin was transferred to a 1.5 mL tube and stored at –20  $^{\circ}$ C as a 10% total input sample from the ChIP reaction. The remaining samples were subjected to immunoprecipitation at 4  $^{\circ}$ C overnight using anti-PPAR $\alpha$  antibody (Santa Cruz Biotechnology, sc-398394). Subsequently, 20  $\mu$ L of ChIP Grade Protein A/G Plus Agarose was added and incubated for 1 h at 4  $^{\circ}$ C on a rocking platform. After resin incubation, the precipitated protein-DNA complexes were eluted, the cross-linking was reversed, and the DNA was purified and subjected to qPCR analysis.

### Single-cell RNA-seq

Following IPA and DSS treatment, murine colon crypts were collected and processed into single-cell suspensions using PBS supplemented with 10% fetal bovine serum (FBS). Cells were encapsulated into droplets and libraries prepared using the 10 $\times$  Genomics platform (Hangzhou Cosmos Wisdom Biotech Co., Ltd.), and libraries were sequenced on an Illumina NextSeq. BCL files were demultiplexed, aligned to mouse mm10 genome, filtered and unique molecular identifier-counted using Cell Ranger software (v7.2.0, 10 $\times$  Genomics)<sup>47</sup>. Then downstream analysis was performed with *Seurat* pipeline (v5.0)<sup>48</sup>. Data filtering was conducted to remove cells with high mitochondrial read percentages (>20%), low ribosomal reads percentages (<1%) and low gene detection counts (<100). The filtered gene expression data were then normalized using the '*NormalizeData*' function with default settings. Following normalization, the top 2000 variable genes were identified using the '*FindVariableFeatures*' function with the '*vst*' method. The expression data of 2000 variable genes underwent scaling and centering analyses using '*ScaleData*' function. Based on the scaled data, we performed principal component analysis (PCA) for dimensionality reduction with the '*RunPCA*' function. Subsequently, t-distributed stochastic neighbor embedding (t-SNE) dimensionality reduction was conducted on the top 10 principal components using the '*RunTSNE*' function. Finally, clustering analyses were performed for all cells using the '*FindNeighbors*' and '*FindClusters*' functions, with a resolution set to 1.4. The '*FindMarkers*' function in the *Seurat* package was utilized to identify differentially expressed genes (DEGs) between the two groups of cells using default parameters. Gene Ontology (GO) and KEGG pathway enrichment analyses for the DEGs were performed using the *ClusterProfiler* R package<sup>49</sup>.

### RNA extraction, library construction, sequencing, and data analyses

Total RNA was extracted from bulk cIECs isolated from mice using TRIzol reagent (Invitrogen). A library was constructed using the ALFA-SEQ RNA Library Prep Kit, following the manufacturer's instructions. Sequencing was performed on an Illumina NovaSeq 6000 platform, producing paired-end reads of 150 bp. The raw reads were filtered to remove unqualified reads using fastp (v0.23.2) software with default settings. The filtered reads were then mapped to the mouse reference genome (GRCm39) using HISAT2 (v2.2.1)<sup>50</sup>. Transcript assembly, gene-mapped read counts, and fragments per kilobase of exon model per million mapped fragments (FPKM) values were generated using StringTie (v3.0.0)<sup>51</sup>. The resulting FPKM profiles were then used as input for *limma* (v3.62.2)<sup>52</sup>. A *P*-value of less than 0.05 and an absolute log<sub>2</sub> FoldChange of less than 0.5 was used as thresholds to identify

significant DEGs. GO and KEGG pathway enrichment analyses were conducted using the *ClusterProfiler* package in the R environment (v4.4.3). Functional categories with a  $P$ -value  $\leq 0.05$  were considered significant, and relevant results were visualized using the *ggplot2* (v3.5.1) package in R.

### Collection and analysis of public metabolomic and metagenomic datasets

A total of three metabolomic public datasets were included for comparative analysis of fecal metabolites between patients and healthy controls (LloydPriceJ\_2019<sup>53</sup>, BushmanFD\_2020<sup>54</sup>, SchirmerM\_2024<sup>55</sup>). The analytical methodology and parameters applied to the metabolomic datasets were consistent with those described above. Additionally, a one-sample t-test was employed to determine whether the  $\text{Log}_2$  Foldchange values of metabolites in all four case-control pairwise comparisons were significantly higher or lower than 0. Meanwhile, four shotgun metagenomic datasets were retrieved and downloaded for re-analysis using a reference-based method (HeQ\_2017<sup>56</sup>, SchirmerM\_2018<sup>57</sup>, LloydPriceJ\_2019<sup>53</sup> and YanQ\_2023c<sup>58</sup>). Following quality control and removal of host-derived reads, high-quality reads from all samples were mapped to the *P. russellii* genome (RT-10B, GCF\_003012055.1) using Minimap2 (v2.26-r1175) with default parameters. The read counts were normalized to counts per million (CPM) to enable cross-sample comparisons. The Wilcoxon rank-sum test was employed to access the significance of differences in the relative abundance of *P. russellii*, and  $P$  values were adjusted using Benjamini–Hochberg method.

### Quantitative real-time PCR

Total RNA from bead-homogenized tissue samples or cell culture was extracted using FreeZol reagent (Vazyme, R711) following the manufacturer's instructions. PCR reactions were performed with HiScript II One Step qRT-PCR SYBR<sup>®</sup>Green Kit (Vazyme) on a Gentier 96R Real-Time PCR System (TIANLONG, Xi'an, China). Transcript levels of the indicated genes were normalized to endogenous control GAPDH for each individual sample using the specific primers listed in the Supplementary Table 1 and quantified using the comparative critical threshold cycle  $2^{-\Delta\Delta\text{CT}}$  method.

### Western blotting

Cells and tissue homogenates were lysed in RIPA buffer containing protease and phosphatase inhibitors. Total proteins were quantified by BCA Protein Assay Kit, separated on 10% SDS-PAGE, and then transferred onto polyvinylidene difluoride membranes (BioRad). The membrane was blocked in blocking buffer (5% BSA in 1×TBST, Tris-buffered saline and Tween-20) and then incubated with primary antibodies overnight at 4 °C. After incubation, the membrane was washed three times with TBST and incubated with HRP-conjugated secondary antibodies. The membrane was washed four times in TBST and visualized using an enhanced chemiluminescence kit (Vazyme, E423-01/02) with a ChemiDoc Touch Gel Imaging System (Bio-Rad). Uncropped and unprocessed scans of all Western blots are provided in the Source data file.

### Tissue histology and immunostaining

Colon 'Swiss rolls' soaked in 4% paraformaldehyde solution were dehydrated, embedded in paraffin, cut into 4- $\mu\text{m}$ -thick sections, and stained with haematoxylin and eosin (H&E) using standard procedures. Slices were evaluated by an experienced pathologist in a blinded manner, and histological scores were assessed based on the following parameters according to previous research: inflammation, epithelial defects, crypt atrophy, dysplasia/neoplasia, and the area affected by dysplasia<sup>9</sup>. For the staining of goblet cells, colon sections were also stained in Alcian blue for 10 to 15 min and dehydrated in 100% alcohol and xylene.

For immunofluorescence (IFA) analysis, deparaffinized colon sections were blocked with 10% normal goat serum for 10 min at room temperature. The slides were then incubated with specific primary antibodies at 4 °C overnight. Antibodies used: anti-IL-6 (1:50, Proteintech, 21865-1-AP), anti-occludin (1:100, Proteintech, 13409-1-AP), anti-Muc2 (1:100, Proteintech, 27675-1-AP), anti-Ki67 (1:250, Abcam, ab16667), anti-LGR5 (1:400, Affinity, DF2816) and anti-HMGCS2 (1:100, ABclonal, A14244). After washing with PBS for three times, the slides were then incubated with fluorescently labeled secondary antibodies (Jackson ImmunoResearch) for additional 2 h at room temperature in dark, and nuclei were stained with DAPI (Roche, Switzerland). TUNEL staining was performed using the In situ Cell Death Detection POD kit (Roche Diagnostics) on the Discovery XT according to the manufacturer's protocol. All analyses were performed using ImageJ software.

### Statistics and reproducibility

All statistical analyses were performed using GraphPad Prism. Unless otherwise stated in the figure legends, data are presented as mean  $\pm$  standard deviation (SD). Differences between two groups were assessed by two-tailed Student's t-test; comparisons among multiple groups were analyzed by one-way ANOVA followed by Tukey's post hoc test. Spearman correlation analysis was applied for correlation assessments. For human cohort data, demographic characteristics were compared using the Chi-squared test and Welch's t-test. A  $P$  value  $< 0.05$  was considered statistically significant, and exact  $n$  values for each experiment are provided in the corresponding figure legends.

Sample sizes (typically 3–6 biological replicates per group) were selected based on established standards in the field and our preliminary data, which indicated that this range was sufficient to detect biologically relevant effects. No statistical method was used for prior sample size calculation. All data generated were included in the analyses, with no exclusions. For animal studies, mice were randomly assigned to experimental groups. Key experimental findings were independently replicated at least three times with consistent results.

### Ethics

This study complies with all relevant ethical regulations. Research involving human participants was approved by the Clinical Research Ethics Committee of Sir Run Run Shaw Hospital, Zhejiang University School of Medicine (Approval No. 20210622-31) and the Clinical Research Ethics Committee of the First Affiliated Hospital of Guangdong Pharmaceutical University (Approval No. V1.0, 20210221). Informed consent was obtained from all human participants.

All animal experiments were approved by the Animal Experimentation Ethics Committee of Zhejiang University (Approval No. 27248) and the IACUC of Shenzhen Gnotobio Biotechnology Co., Ltd. (Approval No. JTAW20240615-1).

### Reporting summary

Further information on research design is available in the Nature Portfolio Reporting Summary linked to this article.

### Data availability

The raw bulk RNA sequencing data and single-cell RNA sequencing data generated in this study have been deposited in the Genome Sequence Archive (GSA) in National Genomics Data Center under accession codes CRA025369 and CRA024086, respectively. The fecal metabolomic profiles generated in this study are provided in the Supplementary Data. The four raw metagenomic datasets analyzed in this study were obtained from the previously published studies and are publicly available at European Nucleotide Archive under the following project accessions: PRJEB15371, PRJNA398089, PRJNA389280, and PRJEB67456. Metabolomic profiles and associated metadata for the three IBD cohorts were also obtained from published studies and are publicly available as follows: for BushmanFD\_2020, data are available

on GitHub (<https://github.com/renyl/cdiff>); for LloydPriceJ\_2019, data are available in the Metabolomics Workbench database under Project ID PR000639; and for SchirmerM\_2024, data were obtained from the supplementary Data of the corresponding publication. The genome sequence and annotation files for *Mus musculus* (GRCm39, release I10) were downloaded from the Ensembl database. The genome of *P. russellii* strain RT-10B was downloaded from the NCBI database under accession number GCF\_003012055.1. Source data are provided with this paper.

## Code availability

The intermediate results, analysis and visualization codes used in this study have been uploaded into the GitHub repository, accessible at <https://github.com/mengjx855/25-IPA-HMGCS2-ISC>.

## References

- Miyoshi, H., Ajima, R., Luo, C. T., Yamaguchi, T. P. & Stappenbeck, T. S. Wnt5a potentiates TGF-beta signaling to promote colonic crypt regeneration after tissue injury. *Science* **338**, 108–113 (2012).
- Barker, N. et al. Identification of stem cells in small intestine and colon by marker gene Lgr5. *Nature* **449**, 1003–1007 (2007).
- Wu, N. et al. MAP3K2-regulated intestinal stromal cells define a distinct stem cell niche. *Nature* **592**, 606–610 (2021).
- Wang, R. et al. Gut stem cell necroptosis by genome instability triggers bowel inflammation. *Nature* **580**, 386–390 (2020).
- Villablanca, E. J., Selin, K. & Hedin, C. R. H. Mechanisms of mucosal healing: treating inflammatory bowel disease without immunosuppression? *Nat. Rev. Gastroenterol. Hepatol.* **19**, 493–507 (2022).
- Pull, S. L., Doherty, J. M., Mills, J. C., Gordon, J. I. & Stappenbeck, T. S. Activated macrophages are an adaptive element of the colonic epithelial progenitor niche necessary for regenerative responses to injury. *Proc. Natl. Acad. Sci. USA* **102**, 99–104 (2005).
- Kaiko, G. E. et al. The colonic crypt protects stem cells from microbiota-derived metabolites. *Cell* **167**, 1137 (2016).
- Peck, B. C. E., Shanahan, M. T., Singh, A. P. & Sethupathy, P. Gut microbial influences on the mammalian intestinal stem cell niche. *Stem Cells Int.* **2017**, 5604727 (2017).
- Zhang, Y. et al. *Dubosiella newyorkensis* modulates immune tolerance in colitis via the L-lysine-activated AhR-IDO1-Kyn pathway. *Nat. Commun.* **15**, 1333 (2024).
- Subramanian, B. C. Inflammatory bowel disease: DCs sense LTβ(4) to drive T(H)1 and T(H)17 differentiation. *Cell Mol. Immunol.* **17**, 307–309 (2020).
- Ayyaz, A. et al. Single-cell transcriptomes of the regenerating intestine reveal a revival stem cell. *Nature* **569**, 121–125 (2019).
- Cheng, C. W. et al. Ketone body signaling mediates intestinal stem cell homeostasis and adaptation to diet. *Cell* **178**, 1115–1131.e1115 (2019).
- Wang, Y. et al. Long-term culture captures injury-repair cycles of colonic stem cells. *Cell* **179**, 1144–1159.e1115 (2019).
- Youm, Y. H. et al. The ketone metabolite beta-hydroxybutyrate blocks NLRP3 inflammasome-mediated inflammatory disease. *Nat. Med.* **21**, 263–269 (2015).
- Grabacka, M., Pierzchalska, M., Dean, M. & Reiss, K. Regulation of ketone body metabolism and the role of PPARα. *Int. J. Mol. Sci.* **17**, 2093 (2016).
- Shao, M. et al. Hepatic IRE1α regulates fasting-induced metabolic adaptive programs through the XBP1s-PPARα axis signaling. *Nat. Commun.* **5**, 3528 (2014).
- Vila-Brau, A., De Sousa-Coelho, A. L., Mayordomo, C., Haro, D. & Marrero, P. F. Human HMGCS2 regulates mitochondrial fatty acid oxidation and GGF21 expression in HepG2 cell line. *J. Biol. Chem.* **286**, 20423–20430 (2011).
- Chen, C. et al. Microbial tryptophan metabolites ameliorate ovariectomy-induced bone loss by repairing intestinal AhR-mediated gut-bone signaling pathway. *Adv. Sci.* **11**, e2404545 (2024).
- Wei, Y. et al. Aryl hydrocarbon receptor activation drives polymorphonuclear myeloid-derived suppressor cell response and efficiently attenuates experimental Sjogren's syndrome. *Cell Mol. Immunol.* **19**, 1361–1372 (2022).
- Gao, H. et al. Microbiota-derived IPA alleviates intestinal mucosal inflammation through upregulating Th1/Th17 cell apoptosis in inflammatory bowel disease. *Gut Microbes* **17**, 2467235 (2025).
- Venkatesh, M. et al. Symbiotic bacterial metabolites regulate gastrointestinal barrier function via the xenobiotic sensor PXR and Toll-like receptor 4. *Immunity* **41**, 296–310 (2014).
- Xiao, H. W. et al. Gut microbiota-derived indole 3-propionic acid protects against radiation toxicity via retaining acyl-CoA-binding protein. *Microbiome* **8**, 69 (2020).
- Flannigan, K. L. et al. The Pregnane X receptor and indole-3-propionic acid shape the intestinal mesenchyme to restrain inflammation and fibrosis. *Cell Mol. Gastroenterol. Hepatol.* **15**, 765–795 (2023).
- Pawlak, M., Lefebvre, P. & Staels, B. Molecular mechanism of PPARα action and its impact on lipid metabolism, inflammation and fibrosis in non-alcoholic fatty liver disease. *J. Hepatol.* **62**, 720–733 (2015).
- Rodriguez, J. C., Gil-Gomez, G., Hegardt, F. G. & Haro, D. Peroxisome proliferator-activated receptor mediates induction of the mitochondrial 3-hydroxy-3-methylglutaryl-CoA synthase gene by fatty acids. *J. Biol. Chem.* **269**, 18767–18772 (1994).
- Agus, A., Planchais, J. & Sokol, H. Gut microbiota regulation of tryptophan metabolism in health and disease. *Cell Host Microbe* **23**, 716–724 (2018).
- Dodd, D. et al. A gut bacterial pathway metabolizes aromatic amino acids into nine circulating metabolites. *Nature* **551**, 648–652 (2017).
- Sinha, A. K. et al. Dietary fibre directs microbial tryptophan metabolism via metabolic interactions in the gut microbiota. *Nat. Microbiol.* **9**, 1964–1978 (2024).
- Wlodarska, M. et al. Indoleacrylic acid produced by commensal peptostreptococcus species suppresses inflammation. *Cell Host Microbe* **22**, 25–37.e26 (2017).
- Jia, D. et al. Microbial metabolite enhances immunotherapy efficacy by modulating T cell stemness in pan-cancer. *Cell* **187**, 1651–1665.e1621 (2024).
- Dmitrieva-Posocco, O. et al. beta-Hydroxybutyrate suppresses colorectal cancer. *Nature* **605**, 160–165 (2022).
- White, Z. et al. Gut inflammation promotes microbiota-specific CD4 T cell-mediated neuroinflammation. *Nature* **643**, 509–518 (2025).
- Roda, G., Jharap, B., Neeraj, N. & Colombel, J. F. Loss of response to anti-TNFs: definition, epidemiology, and management. *Clin. Transl. Gastroenterol.* **7**, e135 (2016).
- Dahmus, J., Rosario, M. & Clarke, K. Risk of lymphoma associated with anti-TNF therapy in patients with inflammatory bowel disease: implications for therapy. *Clin. Exp. Gastroenterol.* **13**, 339–350 (2020).
- Singh, S., Facciorusso, A., Dulai, P. S., Jairath, V. & Sandborn, W. J. Comparative risk of serious infections with biologic and/or immunosuppressive therapy in patients with inflammatory bowel diseases: a systematic review and meta-analysis. *Clin. Gastroenterol. Hepatol.* **18**, 69–81.e63 (2020).
- Fu, Y., Gao, H., Hou, X., Chen, Y. & Xu, K. Pretreatment with IPA ameliorates colitis in mice: colon transcriptome and fecal 16S amplicon profiling. *Front Immunol.* **13**, 1014881 (2022).
- Serger, E. et al. The gut metabolite indole-3 propionate promotes nerve regeneration and repair. *Nature* **607**, 585–592 (2022).
- Jiang, J. et al. The gut metabolite indole-3-propionic acid activates ERK1 to restore social function and hippocampal inhibitory synaptic

- transmission in a 16p11.2 microdeletion mouse model. *Microbiome* **12**, 66 (2024).
39. Perdijk, O. et al. Antibiotic-driven dysbiosis in early life disrupts indole-3-propionic acid production and exacerbates allergic airway inflammation in adulthood. *Immunity* **57**, 1939–1954.e1937 (2024).
  40. Weigmann, B. et al. Isolation and subsequent analysis of murine lamina propria mononuclear cells from colonic tissue. *Nat. Protoc.* **2**, 2307–2311 (2007).
  41. Kirkwood, K. I. et al. Utilizing Skyline to analyze lipidomics data containing liquid chromatography, ion mobility spectrometry and mass spectrometry dimensions. *Nat. Protoc.* **17**, 2415–2430 (2022).
  42. Xu, S. et al. Using clusterProfiler to characterize multiomics data. *Nat. Protoc.* **19**, 3292–3320 (2024).
  43. Robinson, C. E., Wu, X., Morris, D. C. & Gimble, J. M. DNA bending is induced by binding of the peroxisome proliferator-activated receptor gamma 2 heterodimer to its response element in the murine lipoprotein lipase promoter. *Biochem. Biophys. Res. Commun.* **244**, 671–677 (1998).
  44. Yan, Y., Tao, H., He, J. & Huang, S. Y. The HDOCK server for integrated protein-protein docking. *Nat. Protoc.* **15**, 1829–1852 (2020).
  45. Zhao, Z. et al. Hepatic PPARalpha function is controlled by poly-ubiquitination and proteasome-mediated degradation through the coordinated actions of PAQR3 and HUWE1. *Hepatology* **68**, 289–303 (2018).
  46. Sato, T. et al. Single Lgr5 stem cells build crypt-villus structures in vitro without a mesenchymal niche. *Nature* **459**, 262–265 (2009).
  47. Zheng, G. X. et al. Massively parallel digital transcriptional profiling of single cells. *Nat. Commun.* **8**, 14049 (2017).
  48. Hao, Y. et al. Dictionary learning for integrative, multimodal and scalable single-cell analysis. *Nat. Biotechnol.* **42**, 293–304 (2024).
  49. Wu, T. et al. clusterProfiler 4.0: a universal enrichment tool for interpreting omics data. *Innovation* **2**, 100141 (2021).
  50. Kim, D., Paggi, J. M., Park, C., Bennett, C. & Salzberg, S. L. Graph-based genome alignment and genotyping with HISAT2 and HISAT-genotype. *Nat. Biotechnol.* **37**, 907–915 (2019).
  51. Pertea, M. et al. StringTie enables improved reconstruction of a transcriptome from RNA-seq reads. *Nat. Biotechnol.* **33**, 290–295 (2015).
  52. Ritchie, M. E. et al. limma powers differential expression analyses for RNA-sequencing and microarray studies. *Nucleic Acids Res.* **43**, e47 (2015).
  53. Lloyd-Price, J. et al. Multi-omics of the gut microbial ecosystem in inflammatory bowel diseases. *Nature* **569**, 655–662 (2019).
  54. Bushman, F. D. et al. Multi-omic analysis of the interaction between clostridioides difficile infection and pediatric inflammatory bowel disease. *Cell Host Microbe* **28**, 422–433.e427 (2020).
  55. Schirmer, M. et al. Linking microbial genes to plasma and stool metabolites uncovers host-microbial interactions underlying ulcerative colitis disease course. *Cell Host Microbe* **32**, 209–226.e207 (2024).
  56. He, Q. et al. Two distinct metacommunities characterize the gut microbiota in Crohn's disease patients. *Gigascience* **6**, 1–11 (2017).
  57. Schirmer, M. et al. Dynamics of metatranscription in the inflammatory bowel disease gut microbiome. *Nat. Microbiol.* **3**, 337–346 (2018).
  58. Yan, Q. et al. A genomic compendium of cultivated human gut fungi characterizes the gut mycobiome and its relevance to common diseases. *Cell* **187**, 2969–2989.e2924 (2024).
- Qu from Department of Physiology and Pathophysiology, School of Basic Medical Sciences, Capital Medical University for providing valuable *Ppara*-flox mice. We appreciate Dr. Kai Xia from National-Local Joint Engineering Research Center for Stem Cells and Regenerative Medicine, Zhongshan School of Medicine, Sun Yat-sen University for providing *Hmgcs2*-flox mice. We appreciate Dr. Jie Yin from Hunan Agricultural University for providing *Pxr*<sup>-/-</sup> mice. The professional editing service NB Revisions was used for technical preparation of the text prior to submission. This work is supported by grants from the National Natural Science Foundation of China (No. 323B2007, No. 82174467, No. 82572567, and No. 82574811) to Y.Z., S.J.Z., and L.Z.

## Author contributions

S.J.Z. and Y.Z. designed the experiments. Y.Z., S.T., J.W., W.X., W.W., and J.G. performed the experiments. J.M., X.J., and Z.Q. conducted bioinformatics analysis. X.S. collected samples and data. L.Z. provided human colonic biopsies. A.Q. provided mouse strain. S.H. maintained and expanded the mouse strain. S.C. coordinated the project. B.D., Z.Z., P.G., and B.S. commented on and revised drafts of the manuscript. S.J.Z., Y.Z., J.M., and S.T. wrote the paper. S.J.Z. supervised research, coordination, and strategy.

## Competing interests

The authors declare no competing interests.

## Additional information

**Supplementary information** The online version contains supplementary material available at <https://doi.org/10.1038/s41467-026-69341-z>.

**Correspondence** and requests for materials should be addressed to Shu Jeffrey Zhu.

**Peer review information** *Nature Communications* thanks Philip Busbee, Samuel Huber and the other, anonymous, reviewer(s) for their contribution to the peer review of this work. A peer review file is available.

**Reprints and permissions information** is available at <http://www.nature.com/reprints>

**Publisher's note** Springer Nature remains neutral with regard to jurisdictional claims in published maps and institutional affiliations.

**Open Access** This article is licensed under a Creative Commons Attribution-NonCommercial-NoDerivatives 4.0 International License, which permits any non-commercial use, sharing, distribution and reproduction in any medium or format, as long as you give appropriate credit to the original author(s) and the source, provide a link to the Creative Commons licence, and indicate if you modified the licensed material. You do not have permission under this licence to share adapted material derived from this article or parts of it. The images or other third party material in this article are included in the article's Creative Commons licence, unless indicated otherwise in a credit line to the material. If material is not included in the article's Creative Commons licence and your intended use is not permitted by statutory regulation or exceeds the permitted use, you will need to obtain permission directly from the copyright holder. To view a copy of this licence, visit <http://creativecommons.org/licenses/by-nc-nd/4.0/>.

© The Author(s) 2026

## Acknowledgements

We thank Dr. Daqian Xu, Dr. Dingjiacheng Jia and Dr. Yuhao Wang for their valuable comments for the manuscript. We appreciate Dr. Aijuan